

A cyclic bipolar wind in the interacting binary V 393 Scorpii

R.E. Mennickent^{1*}, Z. Kołaczkowski², G. Djurasevic^{3,4}, E. Niemczura², M. Diaz⁵,
M. Curé⁶, I. Araya⁶, G. J. Peters⁷

¹Universidad de Concepción, Departamento de Astronomía, Casilla 160-C, Concepción, Chile

²Instytut Astronomiczny Uniwersytetu Wrocławskiego Ul. Kopernika 11, 51-622 Wrocław, Poland

³Astronomical Observatory, Volgina 7, 11060 Belgrade 38, Serbia

⁴Isaac Newton Institute of Chile, Yugoslavia Branch

⁵Departamento de Astronomia, IAG, U. de Sao Paulo, Rua do Matao, 1226, Butanta 05508-900, Sao Paulo, SP, Brasil

⁶Departamento de Física y Astronomía, Facultad de Ciencias, Universidad de Valparaíso, Chile

⁷Space Sciences Center/Department of Physics & Astronomy, University of Southern California, Los Angeles, CA 90089-1341, USA

ABSTRACT

V 393 Scorpii is a Double Periodic Variable characterized by a relatively stable non-orbital photometric cycle of 253 days. Mennickent et al. argue for the presence of a massive optically thick disc around the more massive B-type component and describe the evolutionary stage of the system. In this paper we analyze the behavior of the main spectroscopic optical lines during the long non-orbital photometric cycle. We study the radial velocity of the donor determining their orbital elements and find a small but significant orbital eccentricity ($e = 0.04$). The donor spectral features are modeled and removed from the spectrum at every observing epoch using the light-curve model given by Mennickent et al. We find that the line emission is larger during eclipses and mostly comes from a bipolar wind. We find that the long cycle is explained in terms of a modulation of the wind strength; the wind has a larger line and continuum emissivity on the high state. We report the discovery of highly variable chromospheric emission in the donor, as revealed by Doppler maps of the emission lines Mg II 4481 and C I 6588. We discuss notable and some novel spectroscopic features like discrete absorption components, especially visible at blue-depressed O I 7773 absorption wings during the second half-cycle, Balmer double emission with V/R -curves showing “Z-type” and “S-type” excursions around secondary and main eclipse, respectively, and $H\beta$ emission wings extending up to $\pm 2000 \text{ km s}^{-1}$. We discuss possible causes for these phenomena and for their modulations with the long cycle.

Key words: stars: early-type, stars: evolution, stars: mass-loss, stars: emission-line, stars: winds-outflows, stars: binaries-eclipsing, stars: variables-others

1 INTRODUCTION

V 393 Scorpii is one of the Galactic Double Periodic Variables (DPVs), a group of interacting binaries showing a long photometric cycle lasting roughly 33 times the orbital period (Mennickent et al. 2003, 2005, 2008, Mennickent & Kołaczkowski 2010, Radek et al. 2010). DPVs have been interpreted as semi-detached interacting binaries ongoing cyclic episodes of mass loss into the interstellar medium (Mennickent et al. 2008, Mennickent & Kołaczkowski 2010). The long photometric cycle of V 393 Sco (253 days) was discovered by Pilecki & Szczygiel (2007) by inspecting the ASAS catalogue of eclipsing binaries with additional variability. Ultraviolet spectra of V 393 Sco were studied by Peters (2001) who

found evidence for a hot temperature region that should be the origin of superionized lines like NV, CIV and SiIV. These lines are likely produced by resonance scattering in a plasma of temperature $T \sim 10^5 \text{ K}$ and electron density $N_e \sim 10^9 \text{ cm}^{-3}$ (Peters & Polidan 1984). Broad band photometry was modeled by Mennickent et al. (2010a, hereafter M10), who found a distance $d = 523 \text{ pc}$ and reddening $E(B - V) = 0.13$. They interpreted observed asymmetries in UV lines of highly ionized metals as evidence for a high-latitude wind. They also studied orbitally-resolved high resolution infrared spectra and found a remarkable depressed blue wing in the He I 1083 nm line near secondary eclipse, that interpreted as evidence of mass loss through the $L3$ point. The relatively stable ultraviolet spectra during the long cycle yielded these authors to suggest that the mass outflow related to the long cycle should be through the equatorial plane.

* E-mail: rmennick@astro-udec.cl. Based on ESO proposal 081.D-0457(B)

Posteriorly, Mennickent et al. (2012, hereafter M12) disentan-

gled the orbital and long-cycle light curves and performed a multi-parametric fit to the orbital light curve considering two stellar components plus a circumprimary disc. The best fit is obtained with a Roche-lobe filling A7 giant (hereafter the donor or secondary star) and a B4 dwarf (the gainer or primary) that is surrounded by an optically thick disc with a radius almost twice the radius of its central star. The disc has 16.600 K in the inner parts and 8.600 K in the outer regions. The orbit is circular with separation $35 R_{\odot}$ and the inclination is 80 degree. M12 found two bright spots in the disc, that are needed to fully reproduce the shape of the orbital light curve. These spots are 20% hotter than the disc and face the observer at orbital phases 0.90 and 0.45.

M12 performed a χ^2 minimization procedure to find the system and orbital parameters that best match a grid of theoretical evolutionary tracks for binary stars including non-conservative processes. After performing this procedure, M12 find an age of 70 Myr, but more importantly, they found that the system is just after a mass transfer burst that transferred $4 M_{\odot}$ from the donor to the gainer in just 400.000 years. The system and orbital parameters are reproduced relatively well, but a mismatch between the gainer dynamical mass and its luminosity is found. In order to explain this discrepancy, M12 argue that not all transferred mass has been accumulated by the (possibly critically rotating) gainer, but a significant fraction ($\sim 2 M_{\odot}$) still remains in the disc. Regarding the long cycle, M12 find that *is not* produced by changes in the relatively stable disc, and invoke a variable high latitude wind as probable cause for the phenomenon. Emission in this wind should explain, according to them, the non-eclipsing nature of the long variability and their red colors at maximum.

With the aim of studying the nature and origin of the long photometric cycle, we carried out a spectroscopic campaign of V 393 Sco using several high resolution spectrographs at different observatories in Chile. Additional spectra taken 20 years ago at Kitt Peak National Observatory were also considered. The analysis of the main spectral features of V 393 Sco is presented in this paper. We postpone for a future paper the analysis of the weaker spectroscopic features.

In this paper long-cycle maximum and minimum are indistinctly named high and low state, respectively. We use the ephemerides for the orbital and long cycles given by M12, viz., the main orbital photometric minimum happens at $HJD_o = 2\,452\,507.7800 + 7.7125772E$ (Kreiner 2004) and the maximum of the long cycle occurs at $HJD_l = 2452522 + 253E$. The observations, instruments and reduction techniques are presented in Section 2, the results are given in Section 3, a general discussion is presented in Section 4 and the conclusions are given in Section 5. A brief preliminary report of this research was published in a conference proceeding by Mennickent et al. (2010b).

2 SPECTROSCOPIC OBSERVATIONS AND DATA REDUCTION

We conducted spectroscopic observations of V 393 Sco during 2 years obtaining optical spectra with resolution $R \sim 40.000$ with several echelle spectrographs in Chile. The instruments used were CORALIE, HARPS and FEROS (La Silla ESO Observatory, 106, 6 and 14 spectra, respectively), UVES (Paranal ESO Observatory, 359 spectra) and DuPont-echelle and MIKE (Las Campanas Ob-

servatory, 42 and 17 spectra, respectively)¹. The studied spectral regions were 3865-6900 Å (CORALIE), 3780-6910 Å (HARPS), 3560-9215 Å (FEROS), 3600-9850 Å (DuPont-echelle) 3350-5000 & 4900-9500 Å (MIKE), 3760-4985, 5682-7520 & 7660-9464 Å (UVES). We also included 9 medium resolution ($R \approx 15.000$) spectra in the H α region and 2 in the He 4471 region ($R \approx 22.000$) obtained between years 1987-1990 with the COUDE spectrograph in the Kitt Peak National Observatory. Since the long-cycle phases are quite uncertain these spectra are only phased with the orbital cycle. In general, their variability is not different from spectra acquired 20 years later. A total of 555 spectra were acquired during our campaign, most of them with signal to noise ratio larger than 100. The histograms for the orbital and long-cycle phases of the high resolution spectra obtained in the H α region show that our observations cover relatively well the short and long periodicity (Fig. 1).

All spectra discussed in this paper are corrected by earth translational motion and normalized to the continuum. The RVs are heliocentric ones. Reductions were done with IRAF² following usual procedures for echelle spectrography, including flat and bias correction, wavelength calibration and order merging. Occasional cleaning of spectra was needed due to the presence of bright features produced by incident cosmic rays or the presence of sharp telluric lines. In order to remove these features, we replaced deviant points from a high order fit to the flux distribution in a short spectral segment with the flux corresponding to the fitting function. Most cosmic ray features and telluric lines were efficiently removed with this technique.

Some of the DuPont spectra showed artifacts around short spectral regions produced by interference of light reflected in the detector inner layers. These “fringes” were identified and the fluxes in the affected regions were interpolated and not considered for the analysis.

The spectra obtained with the CORALIE spectrograph are not sky-subtracted. This condition imposed by the instrumental setup has not effect for radial velocity and line strength measurements, since V 393 Sco is very bright even at full moon and we do not flux-calibrate our spectra. Details for our observational runs are given in Tables 1, 2 and 3.

3 RESULTS

3.1 General spectrum appearance and interstellar reddening

The optical spectral region of V 393 Sco shows Balmer, He I, Si II lines in absorption and sometimes strong emission in H α , suggesting a B-type primary surrounded by a variable gaseous envelope, along with metallic absorption lines, interpreted as signatures of the A-type secondary star. A rapid inspection showed several absorption helium lines varying in width and depth, a fact that is consistent with a non-photospheric origin. The above description suggests the presence of circumstellar matter and it is consistent with the earlier classification of intermediate-mass interacting binary for this system.

¹ Technical descriptions for these spectrographs and their cameras can be found in www.lco.cl/, www.eso.org/sci/facilities/paranal/instruments/ and www.eso.org/sci/facilities/lasilla/instruments/.

² IRAF is distributed by the National Optical Astronomy Observatories, which are operated by the Association of Universities for Research in Astronomy, Inc., under cooperative agreement with the National Science Foundation.

Table 1. Summary of LCO and ESO non-UVES spectroscopic observations. N is number of spectra. The HJD at mid-exposure for the first spectrum of the series is given. Φ_o and Φ_l refer to the orbital and long-cycle phase, respectively.

UT-date	Observatory/Telescope	Instrument	N	exptime (s)	HJD-MID (start)	Φ_o	Φ_l
2007-07-19	LCO/Magellan Clay	MIKE	1	20	2454301.47395	0.5674	0.0335
2007-07-20	LCO/Magellan Clay	MIKE	6	230	2454301.50920	0.5720	0.0336
2007-07-21	LCO/Magellan Clay	MIKE	4	40	2454302.53377	0.7048	0.0377
2007-08-01	LCO/Magellan Clay	MIKE	1	920	2454313.62004	0.1422	0.0816
2007-08-02	LCO/Magellan Clay	MIKE	1	390	2454314.55761	0.2638	0.0852
2007-08-05	LCO/Magellan Clay	MIKE	1	250	2454317.70700	0.6721	0.0977
2007-08-16	LCO/Magellan Clay	MIKE	1	270	2454328.58438	0.0825	0.1406
2007-11-08	LCO/Magellan Clay	MIKE	1	120	2454412.50750	0.9638	0.4724
2007-11-09	LCO/Magellan Clay	MIKE	1	160	2454413.49772	0.0922	0.4763
2008-02-24	LCO/Du Pont	Echelle	8	500	2454520.83187	0.0090	0.9005
2008-02-25	LCO/Du Pont	Echelle	6	500	2454521.83514	0.1391	0.9045
2008-06-15	LCO/Du Pont	Echelle	11	500	2454632.51366	0.4895	0.3420
2009-05-14	LCO/Du Pont	Echelle	7	420	2454965.65937	0.6846	0.6587
2009-06-16	LCO/Du Pont	Echelle	6	540–600	2454998.63019	0.9595	0.7891
2009-08-25	LCO/Du Pont	Echelle	4	540	2455068.57889	0.0289	0.0655
2009-02-26	ESO/ 3.6m	HARPS	1	300	2454888.87719	0.7291	0.3552
2009-02-28	ESO/ 3.6m	HARPS	1	180	2454890.82302	0.9814	0.3629
2010-09-09	ESO/ 3.6m	HARPS	1	180	2455448.51123	0.2900	0.5672
2010-09-27	ESO/ 3.6m	HARPS	1	180	2455467.47358	0.7480	0.6422
2010-09-28	ESO/ 3.6m	HARPS	1	210	2455468.48994	0.8800	0.6462
2010-09-30	ESO/ 3.6m	HARPS	1	250	2455470.47588	0.1380	0.6541
2008-03-16	ESO/2.2m	Feros	3	250–300	2454541.89607	0.7401	0.9838
2008-03-17	ESO/2.2m	Feros	3	300–400	2454542.90141	0.8705	0.9878
2008-03-18	ESO/2.2m	Feros	3	300–400	2454543.89221	0.9989	0.9917
2008-03-19	ESO/2.2m	Feros	2	500	2454544.89839	0.1294	0.9956
2008-03-20	ESO/2.2m	Feros	3	400–500	2454545.89879	0.2591	0.9996
2008-04-06	ESO/EULER	CORALIE	6	900	2454562.82551	0.4538	0.0665
2008-04-07	ESO/EULER	CORALIE	8	1000	2454563.77105	0.5764	0.0702
2008-04-08	ESO/EULER	CORALIE	4	900	2454563.77105	0.5764	0.0702
2008-04-09	ESO/EULER	CORALIE	4	1000	2454565.83190	0.8436	0.0784
2008-04-10	ESO/EULER	CORALIE	1	900	2454566.92395	0.9852	0.0827
2008-05-23	ESO/EULER	CORALIE	2	1000	2454609.84474	0.5502	0.2524
2008-05-24	ESO/EULER	CORALIE	4	1000	2454610.78428	0.6721	0.2561
2008-05-25	ESO/EULER	CORALIE	5	1000	2454611.80897	0.8049	0.2601
2008-05-26	ESO/EULER	CORALIE	7	1000	2454612.77847	0.9306	0.2639
2008-08-19	ESO/EULER	CORALIE	1	600	2454698.53568	0.0498	0.6029
2008-08-20	ESO/EULER	CORALIE	1	600	2454699.48964	0.1734	0.6067
2008-08-21	ESO/EULER	CORALIE	1	600	2454700.47897	0.3017	0.6106
2008-08-22	ESO/EULER	CORALIE	2	600	2454701.63242	0.4513	0.6151
2008-08-23	ESO/EULER	CORALIE	2	600	2454702.64402	0.5824	0.6191
2008-08-24	ESO/EULER	CORALIE	2	600	2454703.59256	0.7054	0.6229
2008-08-25	ESO/EULER	CORALIE	1	600	2454704.48019	0.8205	0.6264
2008-08-26	ESO/EULER	CORALIE	1	600	2454705.50720	0.9537	0.6305
2008-08-28	ESO/EULER	CORALIE	1	600	2454707.51773	0.2144	0.6384
2008-10-01	ESO/EULER	CORALIE	6	600–800	2454741.53378	0.6248	0.7729
2008-10-02	ESO/EULER	CORALIE	3	900–1000	2454742.52995	0.7540	0.7768
2008-10-03	ESO/EULER	CORALIE	4	900	2454743.52755	0.8833	0.7807
2009-04-15	ESO/EULER	CORALIE	1	1800	2454936.90276	0.9560	0.5451
2009-04-16	ESO/EULER	CORALIE	3	1300	2454937.87533	0.0821	0.5489
2009-04-17	ESO/EULER	CORALIE	4	1000	2454938.87689	0.2120	0.5529
2009-05-17	ESO/EULER	CORALIE	11	900	2454968.61926	0.0683	0.6704
2009-05-18	ESO/EULER	CORALIE	9	900	2454969.72474	0.2117	0.6748
2009-05-19	ESO/EULER	CORALIE	12	800	2454970.59597	0.3246	0.6782

The interstellar contribution to the color excess can be determined through the analysis of diffuse interstellar bands (DIBs; Munari 2000, Weselak et al. 2008). We measured equivalent widths of DIBs located at 5780 Å, 5797 Å and 8620 Å, estimating $E(B - V) = 0.15 \pm 0.05$, in agreement with the value $E(B - V) = 0.13 \pm 0.02$ obtained by M10 from the fit to the spectral energy distribution. The above probably excludes significant amounts of dust in the line of

sight to V 393 Scorpii and suggests that the color excess is mainly due to interstellar reddening rather than circumstellar matter.

3.2 The donor’s spectrum and its stellar parameters

In order to find the donor spectral type we compared the spectrum observed at minimum light with a grid of synthetic spectra and

Table 2. Summary of KPNO spectroscopic observations obtained with the Coude spectrograph. One spectrum was obtained per night. Φ_o is the orbital phase.

UT-date	$\Delta\lambda$ (Å)	exptime (s)	HJD	Φ_o
1987-05-03	6520-6695	1800	2446918.93455	0.3595
1987-08-24	6520-6695	2700	2447031.69913	0.9804
1989-04-20	6520-6695	2400	2447636.97037	0.4589
1989-04-21	6520-6695	2700	2447637.92552	0.5827
1989-04-23	6520-6695	2700	2447639.97292	0.8482
1989-04-24	6520-6695	3300	2447640.94252	0.9739
1990-08-19	6520-6695	2000	2448122.68538	0.4359
1990-08-20	4420-4535	2700	2448123.65323	0.5614
1990-08-21	4420-4535	3600	2448124.70935	0.6983
1990-08-22	6520-6695	1800	2448125.65894	0.8214
1989-94-21	6520-6695	2700	2447637.92552	0.5827

looked for the best match in a region dominated by donor spectral features. For the reference spectrum we used the FEROS spectrum at $\Phi_o = 0.000$ obtained on March 18, 2008 (hereafter Φ_o and Φ_l stand for orbital and long cycle phase respectively). The region used for the fit, deployed of hydrogen and helium lines but with several metallic lines, was the region between 4150 and 4290 Å.

To determine the grid of synthetic fluxes we used atmospheric models computed with the line-blanketed LTE ATLAS9 code (Kurucz 1993), which treats line opacity with opacity distribution functions (ODFs). The Kurucz's models are constructed with the assumptions of plane-parallel geometry and hydrostatic and radiative equilibrium of the gas. The synthetic spectra were computed with the SYNTH code (Kurucz 1993). Both codes, ATLAS9 and SYNTH were ported under GNU Linux by Sbordone et al. (2005) and are available online³. The atomic data were taken from Castelli & Hubrig (2004)⁴. The theoretical models were obtained for effective temperatures from 6000 to 10000 K with steps of 100 K and for surface gravities from 2.0 to 4.5 dex with the step of 0.1 dex. Solar and 0.5 dex higher metallicities were taken into account. The grid of synthetic spectra was calculated for five different rotation velocities, $v_{2r} \sin i = 0, 25, 50, 75$ and 100 km s^{-1} .

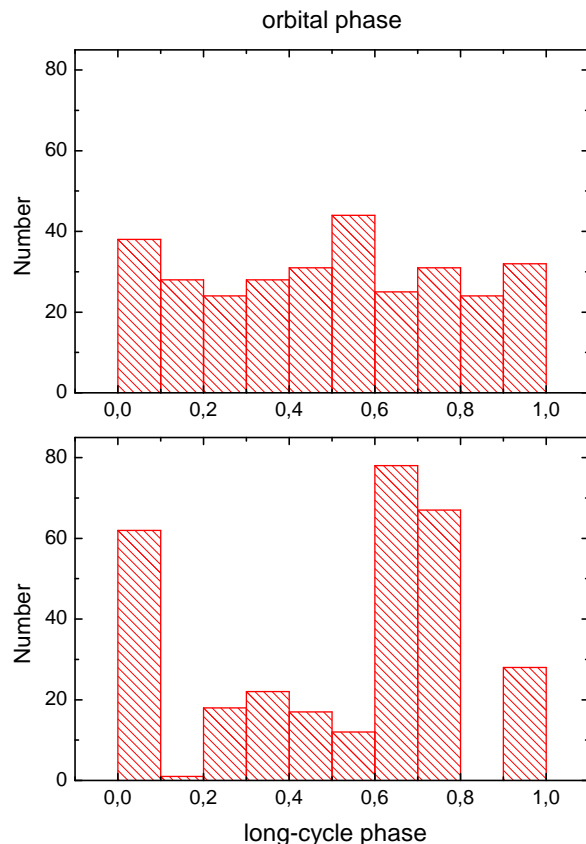
We subtracted the template from every grid spectrum, allowing small wavelength adjustments and analyzed the residuals of the resulting difference spectra. The model with the lower root mean square had $T_2 = 7900 \text{ K}$, $\log g_2 = 3.0$, $v_{2r} \sin i = 75 \text{ km s}^{-1}$ and solar metallicity. Several solar metallicity models with temperatures in the range 7500-8100 K showed similarly small residuals. Some higher metallicity models also fit the spectrum but with higher temperatures, the best one with 8400 K, $\log g = 3.2$, and $v_{2r} \sin i = 75 \text{ km s}^{-1}$. We preferred the lower temperature model for consistency with our earlier calculation and previously published results (M10 and references therein).

From the above we estimate $T_2 = 7900^{+200}_{-400} \text{ K}$. Our low temperature limit is consistent with the absence of the G-band in our spectra. The low sensitivity of spectral features to the donor temperature in the chosen spectral region precludes a better determination of T_2 . Other potential temperature spectral diagnostics like calcium H & K lines could not be used due to contamination with features of other system components.

A refinement of $v_{2r} \sin i$ was done by interpolating the grid of models to the *FWHM* of lines observed on main eclipse, obtain-

Table 3. Summary of observations obtained with the ESO UVES between April 02 and October 01, 2008. N is the number of spectra. The exposure time was 35 s. The complete table is given in electronic form.

N	$\Delta\lambda$ (Å)	HJD range (2450000 +)
119	3760-4985	4558.90352-4740.54141
120	5682-7520	4558.90350-4740.54142
120	7660-9464	4558.90350-4740.54142

**Figure 1.** Number of H α spectra per bin of long and orbital phase.

ing $v_{2r} \sin i = 60 \pm 2 \text{ km s}^{-1}$. A new synthetic model for the donor was constructed using this rotational velocity. This model is used in the rest of this paper. The donor synthetic spectrum compared with a typical UVES spectrum reveals in general a good match except for minor deviations in short wavelength segments due to difficult normalization of the waving continuum (Fig. 2).

Looking at luminosity-sensitive features like the Fe II & Ti II double blend at 4172-8 Å, and similar blends at 4395-4400 Å, 4417 Å and 4444 Å, we do not observe evidence for systematic changes in luminosity for the donor star. The same is true for its temperature, as indicated by line strength ratios.

3.3 Radial velocities for the donor

Radial velocities for the donor were measured by cross-correlating the observed spectra with the FEROS spectrum taken at mid

³ wwwuser.oat.ts.astro.it/atmos/

⁴ <http://wwwuser.oat.ts.astro.it/castelli/grids.html>

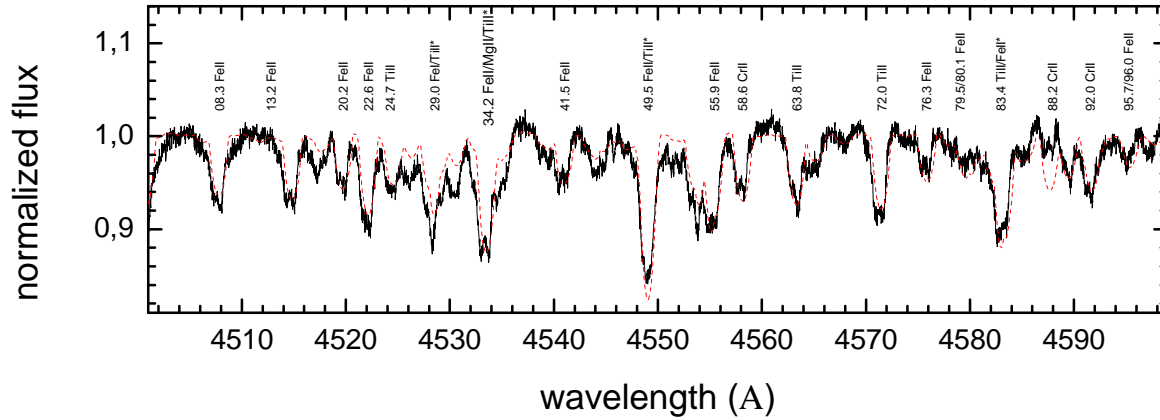


Figure 2. The donor synthetic spectrum (DSS, dashed line) over-plotted with one of our UVES spectrum taken near main eclipse ($\Phi_o = 0.972$, $\Phi_l = 0.753$). To get the DSS, the model synthetic spectrum has been scaled according to the light curve model (M12) to fit the percentage of light contributed by the donor at this epoch. It has also been shifted in wavelength to fit the donor radial velocity at this orbital phase. In the figure, the DSS is vertically shifted to match its continuum with the unity. Metallic lines were identified and labeled ($\lambda - 4500 \text{ \AA}$); uncertain identifications are marked with asterisks.

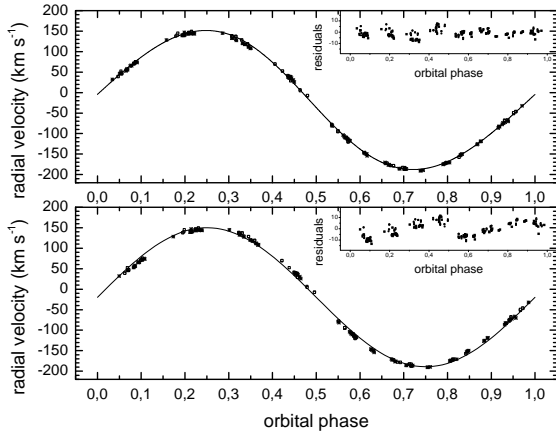


Figure 3. Radial velocities of the donor star (asterisks for CORALIE data and squares for UVES data) and the best fit for elliptical (up) and circular (down) orbits. Residuals are given in the inset graphs.

Table 4. Donor radial velocities obtained by cross-correlation. Labels indicate UVES (U) and CORALIE (C) data. Typical RV error is 1 km s^{-1} . The complete table is given in electronic form.

HJD	RV (km s^{-1})	label
2454558,90258	-55,62	U
2454558,90352	-54,56	U
2454558,90446	-55,59	U
2454559,85331	65,31	U
2454559,85425	65,31	U
2454560,85597	157,97	U
2454560,85691	158,01	U
2454560,85784	157,95	U
2454561,87559	149,95	U
2454561,87653	149,97	U

eclipse. After obtaining relative velocities with respect to this reference spectrum, we applied a zero-point shift considering the template RV, measured by fitting the position of a set of known lines with simple gaussians and comparing these wavelengths with the corresponding laboratory wavelengths. The cross-correlation was performed in two regions deployed of H I and He I lines, viz. 4500–4800 \AA and 5050–5680 \AA . The radial velocities are given in Table 4.

The RVs can be fitted with a sinusoid with radial-velocity half-amplitude $K_2 = 169.7 \pm 0.6 \text{ km s}^{-1}$ and zero point $\gamma = -19.6 \pm 0.4 \text{ km s}^{-1}$. These figures are significantly different from $K_2 = 181 \pm 3$ and $\gamma = -2 \pm 2 \text{ km s}^{-1}$ obtained from the analysis of the single line Mg II 10917 by M10, but this line is probably partly blended with Pa γ and He I 10916 and affected by residual emission. A careful inspection of Fig. 3 shows non-random residuals for the circular fit.

In order to resolve the question about the possible ellipticity of the orbit, we used the genetic algorithm PIKAIA developed by Charbonneau (1995) to find the orbital elements for V 393 Sco. The method consists in finding the set of orbital parameters that produces a series of theoretical velocities that minimize the function χ^2 defined as:

$$\chi^2(P_o, \tau, \omega, e, K_2, \gamma) = \frac{1}{N-6} \sum_{j=1}^N \left(\frac{V_j - V(t_j, P_o, \tau, \omega, e, K_2, \gamma)}{\sigma_j} \right)^2 \quad (1)$$

where N is the number of observations, P_o is the orbital period, ω the periastron longitude, τ the time of passage per the periastron, e the orbital eccentricity, K_2 the half-amplitude of the radial velocity for the donor and γ the velocity of the system center of mass. V_j and V are the observed and theoretical radial velocities at t_j . The theoretical velocity is given by:

$$V(t) = \gamma + K_2(\cos(\omega + v(t)) + e \cos(\omega)) \quad (2)$$

where v is the angular velocity around the system center of mass obtained resolving the following two equations involving the

Table 5. Orbital elements for the donor of V 393 Scorpii obtained by minimization of the χ^2 parameter given by Eq. (1) for the cases of circular (Case C) and elliptical (Case E) orbits. The value $\tau^* = \tau - 2454507.78$ is given and also the error measured as half the difference between the maximum and minimum quantity in one isophote 1σ .

Case	P_o (days)	τ^*	e	ω	K_2 (km s $^{-1}$)	γ (km s $^{-1}$)	χ^2
C	7.7139	9.6	0.00	1.95	170.7	-19.1	9
E	7.7130	1.3	0.04	1.49	169.7	-18.6	2
error	0.0020	0.1	0.02	0.08	2.0	2.8	-

eccentric anomaly E :

$$\tan\left(\frac{v}{2}\right) = \sqrt{\frac{1+e}{1-e}} \tan\left(\frac{E}{2}\right) \quad (3)$$

$$E - e \sin(E) = \frac{2\pi}{P_o}(t - \tau) \quad (4)$$

A range of physically reasonable parameters need to be considered so that the method works. For the period we used the range 0-10 days, the eccentricity was set between 0 and 1, ω between 0 and 2π , τ between the minimum julian day and this value plus P_o , K_2 between 0 and $(V_{max} - V_{min})$ and γ between V_{min} and V_{max} .

The most reliable way to get error estimates for this genetic algorithm is by Monte Carlo simulations, specifically by perturbing the best fit solution and computing the χ^2 of these perturbed solutions. To find the standard deviation region (σ) encompassed by the joint variation of two parameters with all other parameters at their optimized values, we draw the contour corresponding to that value of $\Delta\chi^2$ for 2 degrees of freedom that includes 68.3% of the probability. In our case this corresponds to $\Delta\chi^2 = 2.30$ (Bevington & Robinson 1992, Chapter 11, pp. 212).

The best orbital elements for the circular and eccentric solutions along with their estimated errors are presented in Table 5. It is clear from the χ^2 value in this table and the residual plots in Fig. 3 that the elliptical solution provides the best fit, since it gives residuals without systematic trends and also the smaller χ^2 value. We note that our eccentric solution gives a small e value (0.042) but it is highly significant, according to the statistical test “ p_1 ” of Lucy (2005).

It has been pointed out that gas stream and circumstellar matter can distort spectroscopic features in semi-detached interacting binaries, producing skewed radial velocities and artificial small eccentricities (e.g. Lucy 2005). For a non-interacting binary with the stellar and orbital parameters of V 393 Sco, dynamical tides should have circularized the orbit and synchronized the rotational periods (Zahn 1975, 1977). This should imply that the observed small eccentricity is very likely spurious. However, the system is probably found with a massive circumprimary disc remanent of a recent mass transfer burst and with the primary rotating at critical velocity (M12). It is possible that the observed eccentricity could be the result of a dynamical perturbation introduced by the circumprimary massive disc. This is an open question we let for a future investigation.

3.4 The He I 5875 line and the mass ratio

Radial velocities for He I 5875 were measured using simple gaussian fits. The corresponding spectral region is virtually uncontaminated by donor spectral features. The RVs are in anti-phase

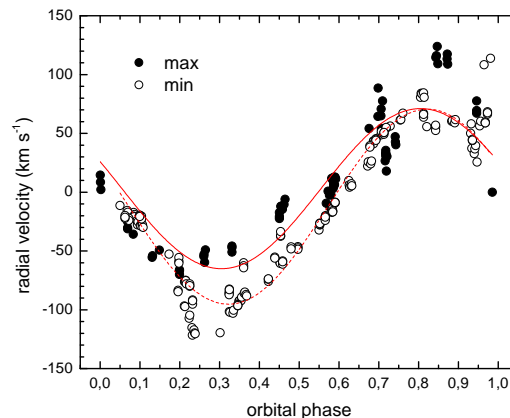


Figure 4. Up: He I 5875 radial velocities at different long cycle phases, $0.2 < \Phi_l \leq 0.8$ (circles) and $0.8 < \Phi_l \leq 0.2$ (dots) and the best sinus fits.

with the donor RVs, revealing their origin in or around the primary star (Fig. 4). There are large RV dispersion at a given phase, and the overall pattern of the RV curve changes during the long-cycle. This fact suggests that He I lines could be affected by residual emission at some epochs. It is therefore difficult to estimate the gainer radial velocity half-amplitude K_1 and the mass ratio from these RVs. We notice, however, that the half-amplitudes are 82.9 ± 1.5 and 68.1 ± 4.5 km s $^{-1}$ at low and high state, respectively (Table 6), much larger than $K_1 = 45.6 \pm 4.6$ km s $^{-1}$ derived from the study of UV and IR lines by M10. If we assume that these half-amplitudes represent the motion of the more massive star then the larger values indicate a mass ratio $q \equiv M_2/M_1 \approx 0.4$ or 0.5 , whereas the M10 figure indicates $q = 0.27 \pm 0.03$. M10 preferred the lower value for the mass ratio since: (i) it allows the formation of a disc around the gainer and (ii) it is more compatible with the mass derived for the secondary star. We add a third reason: (iii) a low mass ratio value is compatible with synchronous rotation for the secondary star. In fact, for a secondary star corotating with the binary:

$$\frac{v_{2r} \sin i}{K_2} \approx (1 + q) \frac{0.49q^{2/3}}{0.6q^{2/3} + \ln(1+q^{1/3})} \quad (5)$$

(Eggleton 2006, Eq. 3.9), where K_2 is the donor radial velocity half-amplitude. Using the above equation, $K_2 = 170$ km s $^{-1}$ and $v_{2r} \sin i = 60$ km s $^{-1}$, we obtain $q \approx 0.27$, consisting with the low q found by M10.

The strength and shape of the He I 5875 line vary during the orbital and long cycles. The $FWHM$ increases systematically from $\Phi_l = 0.5$ to $\Phi_l = 0.0$ and decreases from high to low state. The $FWHM$ increases during the orbital cycle attaining a maximum at $\Phi_o = 0.9$, similarly to He I 10830 (M10). The amplitude of the $FWHM$ variability is about 200 km s $^{-1}$. Emission at the flanks of the He 5875 absorption line is seen occasionally, with typical full peak separation $\Delta\lambda_{5875} \sim 700$ km s $^{-1}$.

The long-cycle variability can be explained by filling emission increasing toward the high state. At low state we observe the deeper and narrower line, and at high state the line is almost filled by emission, producing the observed $FWHM$ increase. Accordingly, the equivalent width (EW) of this line anti-correlates with their $FWHM$. The maximum at $\Phi_o = 0.9$ is produced by an enhanced red absorption wing. This event coincides with the passage

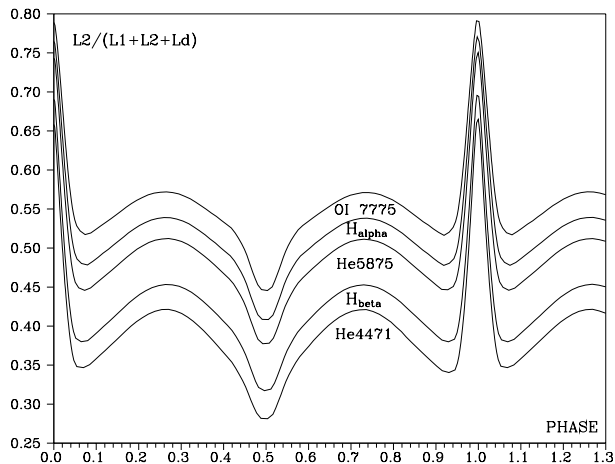


Figure 5. Light contribution factor for the donor at different spectral lines and orbital phases according to the M12 model. L_1 , L_2 and L_d are the gainer, donor and disc fluxes, respectively.

of the hot spot across the line of sight. It could reflect large infall velocities in the absorbing material of the gas stream.

3.5 Spectral disentangling and donor-subtracted spectra

The variable and multicomponent nature of the spectra make difficult their analysis and requires some kind of useful approximation to isolate single component contributions. In order to remove the donor light from the spectra we assume that its contribution to the total light is additive to the other light sources and represented by the model proposed by M12, i.e. it is independent of the long cycle. This assumption is justified because: (i) the amplitude of the long cycle is small compared with the large magnitude changes observed during the orbital cycle and (ii) we do not detect large systematic changes of the donor during the long cycle.

We constructed donor-subtracted spectra by removing the synthetic spectrum of the donor from the observed spectrum. Firstly, the synthetic spectrum was Doppler corrected and scaled according to the contribution of the secondary star at a given orbital phase and at the given wavelength range. For normalized fluxes:

$$f_{res}(\lambda, \Phi_o, \Phi_l) = f(\lambda, \Phi_o, \Phi_l) - p(\Phi_o, \lambda_c) \times f_d(\lambda, \Phi_o) \quad (6)$$

where f_{res} is the donor-subtracted flux, f the observed flux, f_d the synthetic donor spectrum, p is the fractional contribution of the donor derived from our model and λ_c the representative wavelength where this factor is calculated. Theoretical p -factors correctly account for the variable projected area of the donor and its larger flux contribution at longer wavelengths (Fig. 5). The method described above effectively removed the main contribution of the donor to the observed spectra. The result was a set of “donor-subtracted” spectra that were normalized to the new continuum.

Disentangling of the gainer and the disc was not intended since there are no model available for the disc spectral distribution and probably its spectrum combine in a complex way with the spectrum of the primary.

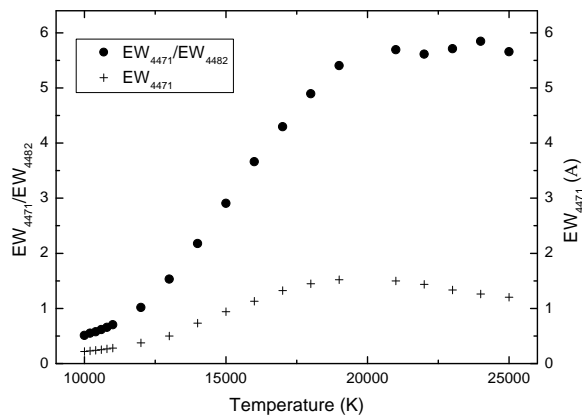


Figure 6. Equivalent widths and equivalent width ratios for synthetic spectra calculated for stellar atmospheres with $\log g = 4.0$, $V_{turb} = 2 \text{ km s}^{-1}$ and solar metallicity.

3.6 The He I 4471 and Mg II 4482 lines

The ratio between the equivalent width of He I 4471 and Mg II 4482 is a good temperature indicator in early B-type stellar atmospheres, being larger for late B-type stars. We calculated equivalent widths and equivalent width ratios (R) as a function of stellar effective temperature for our grid of synthetic stellar spectra (Fig. 6). These calculations are useful to get some insight on the physical conditions of the region forming the helium absorption.

EW_{4471} and R show orbital and long-cycle variability. During high state magnesium emission increases faster, producing a larger R at this state (Fig. 7). This result suggests the R could be used as a rough diagnostic for the long cycle stage in absence of a clear ephemeris, for old spectroscopic observations for instance. The orbital variability of R and EW_{4471} at low state suggests that the effective temperature for the hot component varies with the orbital phase and it is larger at $\Phi_o = 0.4$. At low state EW_{4471} and R are compatible with line formation in a photosphere with $T_{hot} = 16.000 \text{ K}$. This is the same temperature found for the inner disc region (and the gainer) by M12. In contrast, at high state R is larger than any theoretical value, mostly due to the weakness of the magnesium line by filling emission. This makes uncertain any R -based temperature at this stage.

3.7 Balmer and He I 6678 lines

3.7.1 General considerations

According to the M12 model, at $\Phi_o = 0.5$ occurs the largest occultation of the donor by the disc, that attains maximum visibility. We compare $H\alpha$ and He I 6678 Å profiles at this phase for several long-cycle epochs and conclude that (Fig. 8): (i) at low state $H\alpha$ shows a relatively narrow and deep central absorption (CA) flanked by emission peaks of similar intensity. CA is up to 65% the continuum level at this orbital phase, (ii) when the system goes to high state the global emission strength increases and the CA tends to disappear. After a careful examination of the whole dataset, we concluded that this behavior produces the variability of the peak separation described later, i.e., the stronger the CA, the larger the peak separation. Some flat-topped profiles observed at long maximum fit this tendency.

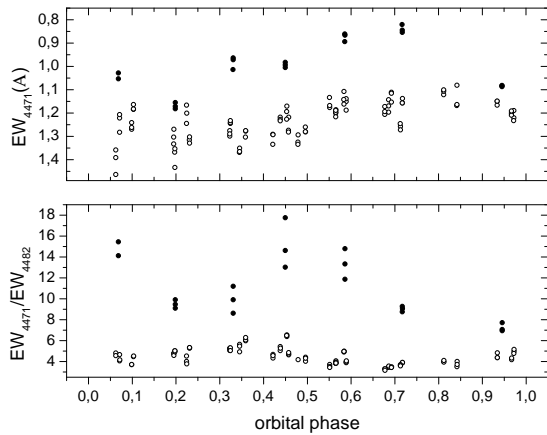


Figure 7. He 4471 equivalent width and He 4471/Mg II 4482 equivalent width ratio versus orbital phase. UVES data for $0.8 < \Phi_l < 0.2$ (filled circles) and $0.2 \leq \Phi_l \leq 0.8$ (open circles) are shown.

We compare theoretical photospheric spectra for a critically rotating gainer with the observed $H\alpha$ and He I 6678 central absorption profiles and conclude that they do not match at long cycle minimum (Fig. 8). However, at high state the He I profile fits the theoretical profile of a slower gainer. We propose that this result is only the consequence of the evident filling emission. In this view the broadening of 200 km s^{-1} probably reflects the kinematics of the gainer pseudo-photosphere. Others interesting features observed in these spectra are the $H\alpha$ emission wings extending beyond 1000 km s^{-1} (see Section 4.2).

The general variability for these lines is illustrated in Fig. 9. The helium line is filled by emission at high state, a characteristic also seen in other helium lines. It is notable the presence of emission flanks with $\Delta\lambda_{6678} \sim 900 \text{ km s}^{-1}$. These flanks are also seen with varying intensity in other helium lines.

The $H\alpha$ line appears as a deep absorption surrounded by weak emission shoulders during low state but it is a strong and double emission (or in few occasions triple or irregular) during high state. For double emission lines the violet emission peak changes its relative intensity with respect to the red peak during the orbital cycle. This property is measured through the V/R ratio, where V is the violet peak intensity and R the red peak intensity. The $V > R$ condition near $\Phi_o = 0.75$ reveals a larger $H\alpha$ emitting region at the binary hemisphere containing the hot spot (Fig. 9). Note also in Fig. 9 the presence of a weak emission line redward $H\alpha$ that we identified with CI 6588. This line follows the donor RV curve and will be discussed in Section 3.9.2.

The $H\beta$ and $H\gamma$ emission profiles show similar behavior to $H\alpha$, but with weaker emission and most importantly with very extended emission wings (EEWs), beyond $\pm 2000 \text{ km s}^{-1}$ (Fig. 10). These velocities are too large to be explained in terms of Keplerian rotation around the gainer. The EEWs usually appear at the red profile flank during the first half of the orbital cycle and at the blue flank during the 2nd half, consisting with an emitting region in the binary hemisphere containing the hot spot, a region high enough to be observed as an emitting source rather than an absorbing media. As occurs with the low-velocity Balmer line emission, the strength of these EEWs is larger at high state.

Occasionally we observe a narrow emission feature redward He I 4921 that is sometimes accompanied with a redshifted absorp-

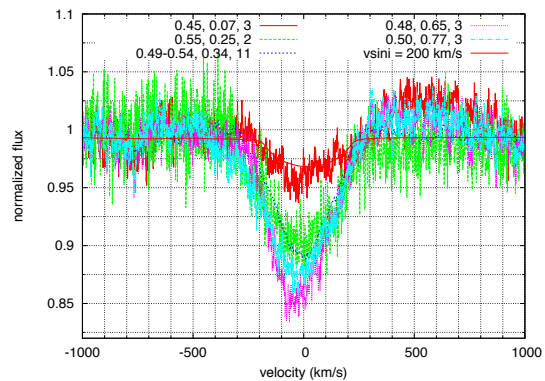
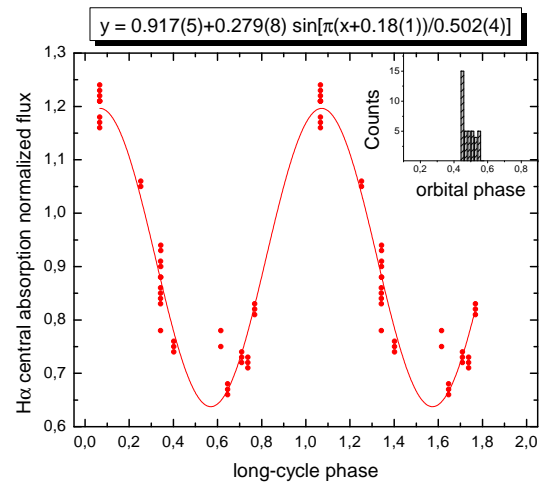
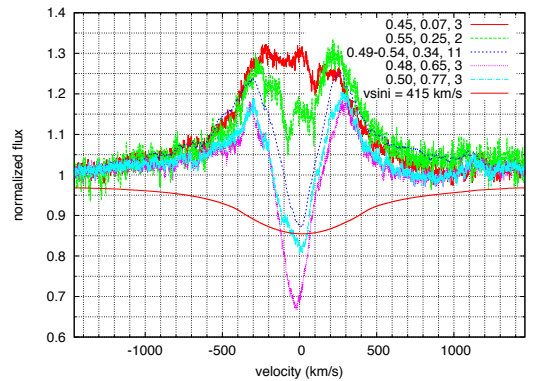


Figure 8. Up and down: Donor-subtracted $H\alpha$ and He I 6678 profiles near secondary eclipse at different long cycle phases. Labels indicate, from left to right, orbital phase, long cycle phase and number of spectra averaged. Synthetic profiles of the gainer calculated with parameters given by M12 are shown for different rotational velocities. X-axis velocities are with respect to the system center of mass. Middle: The behavior of the intensity of the central absorption of the donor-subtracted $H\alpha$ profile at secondary eclipse during the long cycle. The best sinus fit is also shown along with the histogram of orbital phases for the considered spectra.

Table 6. Results of the sinusoidal fits ($\gamma + K \sin(2\pi(x - \delta))$) to the central absorption RV curves. The root mean square of the fit is also given. The parameters γ , K and rms are given in km s^{-1} .

Line (state)	γ	K	δ	rms
H α (all)	-7.9 ± 1.5	59.6 ± 2.3	0.550 ± 0.005	20.1
H β (low)	-9.8 ± 1.0	64.0 ± 1.5	0.546 ± 0.004	15.1
H β (high)	-4.1 ± 3.5	78.4 ± 5.4	0.525 ± 0.009	32.1
H γ (low)	-15.8 ± 1.1	71.3 ± 1.5	0.529 ± 0.003	14.7
H γ (high)	-14.8 ± 2.7	83.2 ± 4.4	0.517 ± 0.006	26.6
O I 7773 (low)	-13.5 ± 2.6	32.1 ± 3.8	0.593 ± 0.017	20.7
He I 5875 (low)	-12.3 ± 1.1	82.9 ± 1.6	0.572 ± 0.003	15.3
He I 5875 (high)	3.0 ± 3.1	68.1 ± 4.5	0.555 ± 0.010	25.0
He I 6678 (all)	-8.8 ± 1.3	70.2 ± 1.9	0.554 ± 0.004	21.6

tion (Fig. 10). We identify this feature as CI4932; its RV suggests an origin in or around the secondary star. This line will be discussed along with other weak spectroscopic features in a forthcoming paper.

3.7.2 Radial velocities of emission line features

Here we present the analysis of the radial velocities of the central cores and emission peaks of the Balmer lines and some helium lines. The CA RV curves were fitted with sinus functions with the best fitting parameters given in Table 6. In general, the radial velocities for Balmer and helium features are in anti-phase with the donor RVs, indicating an origin somewhere near the gainer (Figs. 11 and 12). However, they do not follow the expected motion of the gainer. The half-amplitudes are usually larger than the adopted K_1 value and the positions of the light-centers, as measured by the δ parameters, are displaced from the center of the primary. We notice larger Balmer amplitudes during high state and the opposite for Helium lines. We also notice the relatively small amplitude of the O I 7773 line. The line centers, as measured by the γ parameter, have larger velocity than the systemic velocity, which can be interpreted in terms of an outflow or wind.

Contrary to He 5875, the He I 6678 CA shows small changes through the long cycle. The RV of the blue emission peak shows a quasi-sinusoidal behavior with large amplitude, whereas the red peak remains almost stationary at 390 km s^{-1} shifting to 550 km s^{-1} at high state. On low state the blue H α emission peak shows a large blueshift at $\Phi_o = 0.25$, as occurs with He I 5875 (Fig. 4). This might be due to the approach of the bright spot at longitude 162° (M12). Another notable feature is the shift to bluer wavelengths of the H α CA around $\Phi_o = 0.15$, as corroborated by data obtained on high state at 3 different observatories. This anomaly is also observed in the asymmetric absorption wings discussed in Section 4.5.

If we use the system inclination $i = 80^\circ$ (M12), and the basic kinematics formula:

$$\frac{r}{R_\odot} = \frac{Pv}{50.633} \quad (7)$$

where r represents the radial distance from the center of rotation, P the rotational period in days and v the linear orbital velocity of material moving in the orbital plane measured in km s^{-1} , then we can find the position of the light-centers of the lines listed in Table 6. We find all line light centers located practically in the line joining the stellar centers. In addition, light centers for Balmer and helium lines are located between 9 and 13 R_\odot from the barycen-

ter measured in the direction of the gainer; for O I 7773 this figure is $4.9 R_\odot$. Remembering that the center of mass is located at $7.16 R_\odot$ from the gainer and that this star has a radius of $4.4 R_\odot$ (M12), these results show that all lines are formed somewhere around the gainer, O I 7773 probably near the gainer hemisphere facing the donor (consistent with the location of the DACs forming region) and the other lines in more distant regions. Since the gas dynamics is very likely not limited to the orbital plane and includes important vertical motions not considered in this analysis we should take these results with caution.

3.7.3 Equivalent widths and peak separations

On low state the equivalent width of the He I 6678 line shows large orbital variability and increasing emission during the main eclipse (see Fig. 11, similar behavior is observed in He I 4471 in Fig. 7). This simple observation reveals that the source of the line emission is not eclipsed as occurs with the continuum flux of the donor-subtracted spectra. Interestingly, the same parameter shows much weaker orbital variability on high state, and importantly the strong variability during eclipse disappears. This behavior is difficult to understand, but it could be partly explained if the extra continuum light present at the high state is not eclipsed. In other words, the wind not only contributes to line emission at low/high state but also to continuum emission at high state, i.e. it is optically thicker during the long maximum.

As mentioned before, the H α peak separation is smaller at high state, principally due to the weaker CA. Moreover, the equivalent width of Balmer lines vary during the long cycle in anti-correlation with the peak separation (Fig. 13). The H α peak separation goes from 690 at low state to 340 km s^{-1} at high state, where it cannot be due to Keplerian motions since it should imply an orbit outside the gainer Roche lobe. For H β and H γ the corresponding figures are 800 to 500 km s^{-1} and 1000 to 650 km s^{-1} , respectively. This behavior is opposite to the observed in He 6678, where the peak separation increases on high state (Fig. 10).

If the CA is formed in the gainer disc-like extended photosphere, then we can reasonably assume that rotational broadening determines the CA width, and also indirectly the peak separation. The maximum rotational velocity in the disc is derived from $\Delta\lambda_\gamma$ at low state (about 500 km s^{-1}) and suggests that the primary is in fact rotating at critical velocity. As for helium lines, the Balmer emission increases during main eclipse, indicating that the main source for Balmer line emission is not eclipsed neither. We measure maximum equivalent widths at main eclipse of -40 , -20 and -20 \AA , for H α , H β and H γ , respectively (Fig. 14).

3.7.4 H α V/R variability

The H α V/R ratio follows a quasi-sinusoidal pattern during the orbital cycle with local maxima at $\Phi_o = 0.05$, 0.45 and 0.70 (Fig. 15). In the same figure a reference sinusoid represents the smoothed orbital V/R variability. This variability can be explained by the displacement of the CA across a stationary emission profile. This view is difficult to test measuring the supposedly stationary profile extension, due to their strength variability and gradual merging with the continuum, but it is supported by the fact that the $V < R$ branch coincides with the blue-shifted CA position and the $V > R$ one with the red-shifted. The stability of the V/R curve at high and low state reflects the stability of the disc where the CA is formed, a result also supported by our light-curve photometric model (M12).

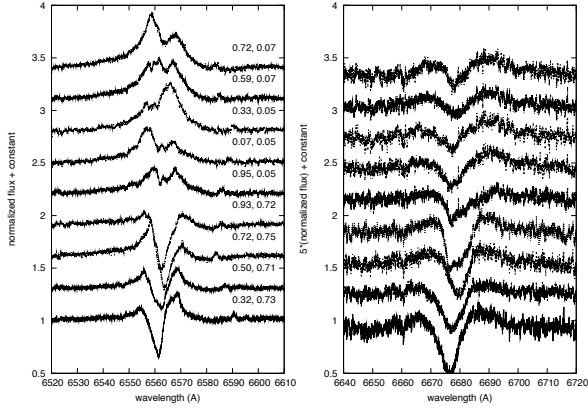


Figure 9. Donor-subtracted H α (left) and He I 6678 (right) spectra at selected epochs. Orbital phases (left) and long-cycle phases (right) are given. Note the C I 6588 emission redward H α .

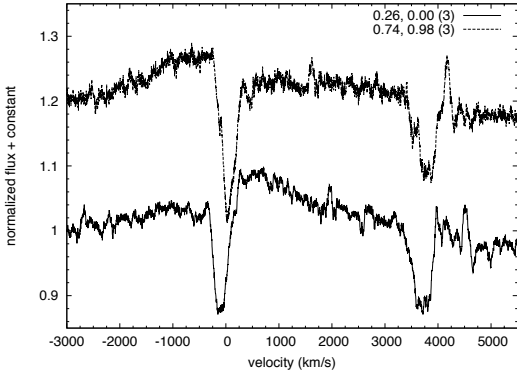


Figure 10. Donor subtracted spectra showing H β extended emission wings up to $\pm 2500 \text{ km s}^{-1}$. The He I 4921 absorption line is also visible along with narrow C I 4932 emission. The numbers between parenthesis indicate the number of averaged spectra.

The zero point of the V/R curve is larger than unity, indicating the predominance of the $V > R$ condition. This is consistent with an outflow of the emitting region, as also indicated by the γ values in Table 6. The V/R curve shows 3 enigmatic successive and rapid reversals just after main eclipse. In addition, a “s-type” variation is found around the referential sinusoid between $\Phi_o = 0.7$ -1.2 and a “z-type” perturbation between $\Phi_o = 0.4$ -0.7.

In order to interpret the s-type and z-type waves, we assume that the high latitude region responsible for Balmer emission extends to the disc of such way that the lower parts merge with the disc bringing its rotational velocity. In this case the s-wave can be viewed as the eclipse of the approaching disc edge by the donor during $\Phi_o = 0.7$ -1.0 and the eclipse of the receding edge during $\Phi_o = 0.0$ -0.2. In the same picture the z-wave probably shows the eclipse by the disc of the receding (approaching) hot spot region in $\Phi_o = 0.4$ -0.5 (0.5-0.6). We remember that according to the light curve model a hot spot is expected in the place where the gas stream hits the disc. This hot spot faces the observer at $\Phi_o = 0.9$ (M12) and

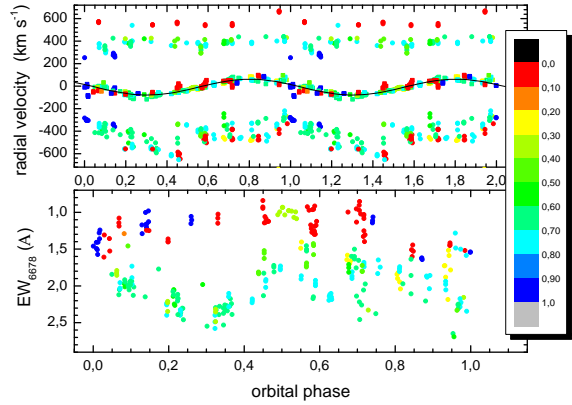


Figure 11. Up: Radial velocity for the central absorption and the red and blue peaks of the He I 6678 line. The best sinus fit for the central absorption is also shown. Down: The equivalent width for the He I 6678 as a function of the orbital and long cycle phase. The color band represents Φ_l ranges.

probably produces, as already mentioned, the $FWHM_{5875}$ peak at $\Phi_o = 0.9$.

In summary, our observations seems to indicate that a wind is emerging from the disc producing Balmer emission lines by electronic recombination. We notice that while our wind-disc model explains well the Balmer line variability, the alternative hypothesis of a circumbinary disc cannot explain many of the observed features.

3.8 Balmer difference spectra

In order to analyze the variable line emission we constructed *difference spectra* by subtracting profiles from a reference profile obtained roughly at the same orbital phase but different long cycle phase, usually that one with the minor line emissivity. We do not correct for the underlying variability of the continuum through the long cycle, since it should have a minor effect on line profile intensity. Difference spectra constitute useful representations of line emission changes at a given orbital phase and projected velocity bin during the long cycle. The results for H α discussed here are basically the same that for H β and H γ .

All difference spectra for H α taken around $\Phi_o = 0.0$ indicate that the emission grows principally at low projected velocities when the system approaches the high state (Fig. 16). The characteristic single peak profile of the extra emission does not correspond with disc emission, either circumprimary or circumbinary and reinforces the thesis of a wind.

At $\Phi_o = 0.75$ the emission grows around -200 km s^{-1} and 50 km s^{-1} (Fig. 16). These velocities suggest that emitting material exist around the donor and the primary, a fact corroborated by the H α Doppler map later. In general, Balmer difference spectra show that the wind line emissivity increases on the high state.

3.9 Doppler Tomography

Doppler tomography was introduced as a tool for the study of accretion discs by Marsh & Horne (1988). This analysis method is now a widespread procedure in the study of emission lines in Al-gols (Richards 2004), and provides a quantitative mapping of optically thin line forming regions in the velocity space. When severe

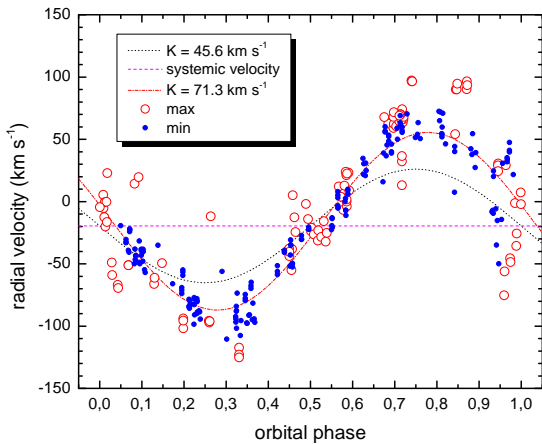
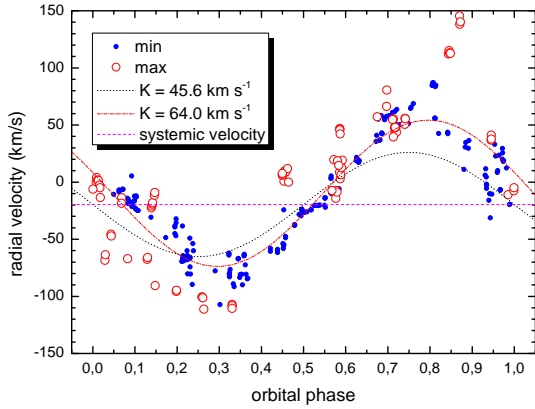
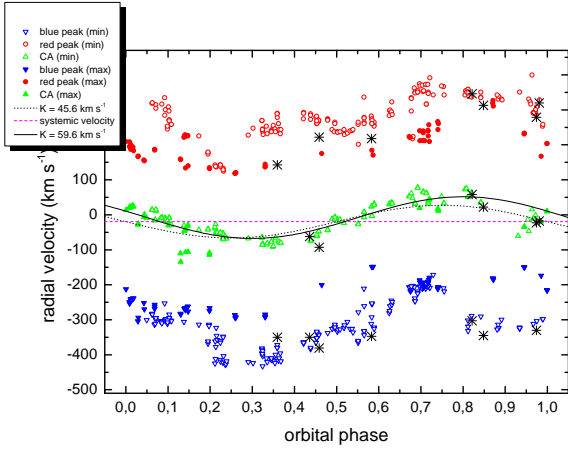


Figure 12. Up: Radial velocity for the blue and red peak of the $H\alpha$ emission and the central absorption. The best sinus fit (excluding outliers around $\Phi_o = 0.15$) along with the assumed track for the gainer are also shown. KPNO data are shown as asterisks and are not included in the fit. Middle and Down: The radial velocity for the $H\beta$ (middle) and $H\gamma$ (down) central absorption. The best sinus fits on low state are shown, along with the assumed track for the gainer. In all graph data for $0.8 < \Phi_l < 0.2$ (max) and $0.2 \leq \Phi_l \leq 0.8$ (min) are shown with separated symbols.

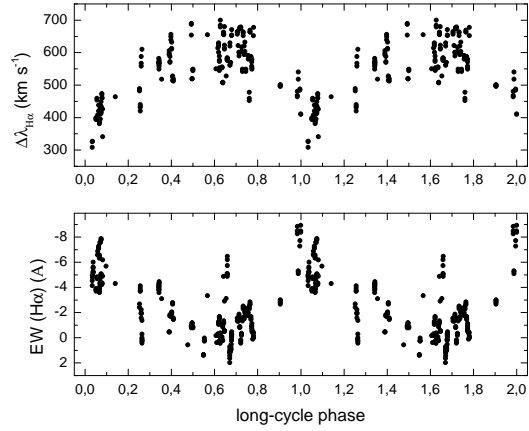


Figure 13. The peak separation (up) and equivalent width (down) of the donor-subtracted $H\alpha$ line profile. Data for $0.95 < \Phi_o < 1.05$ are not shown.

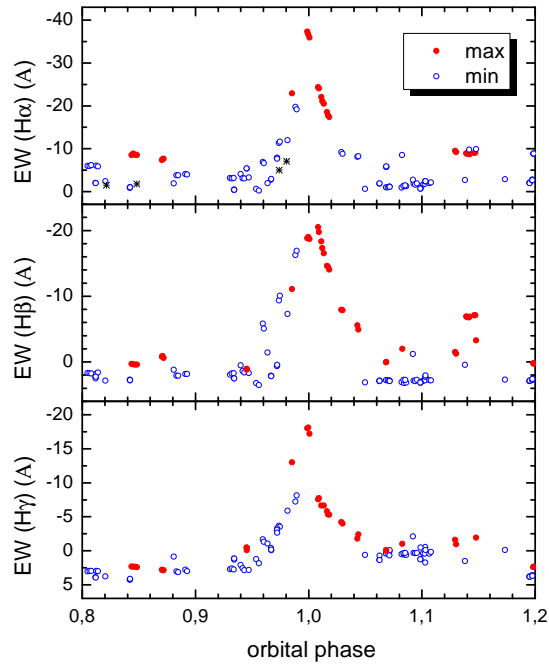


Figure 14. The equivalent width of the donor-subtracted Balmer line profiles during main eclipse. Data on the long cycle phases $0.8 < \Phi_l < 0.2$ are shown as filled circles and those with $0.2 \leq \Phi_l \leq 0.8$ as open circles. Asterisks indicate KPNO data.

self-absorption and/or intrinsic line broadening are present then the tomograms provide at least a concise and convenient way of displaying phase-resolved line profile measurements. The Doppler reconstructions presented in this paper were computed using the filtered back-projection method (Rosenfeld & Kak 1982). The two-dimensional reconstruction of structures in the orbital plane has a unique solution that depends only on the two-dimensional data set (i.e. $f_v(\Phi_o, \lambda)$ where f_v is the flux). Our code has been successfully applied in a number of cases (e.g. Mennickent, Diaz & Arenas

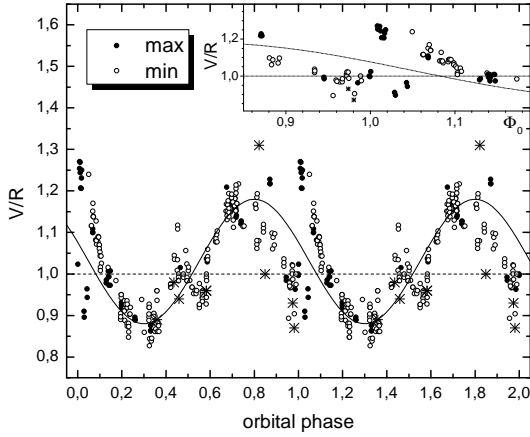


Figure 15. The ratio between the violet and red peak intensity of the donor-subtracted $H\alpha$ double emission profiles (the inset shows a zoom around the main eclipse). The sinusoid $V/R = 1.03 - 0.15 \sin(2\pi(\Phi_o - 0.05))$ has been plotted as reference. Data with $0.8 < \Phi_l < 0.2$ (max) are shown as filled circles and those with $0.2 \leq \Phi_l \leq 0.8$ (min) with open circles. Asterisks indicate KPNO data.

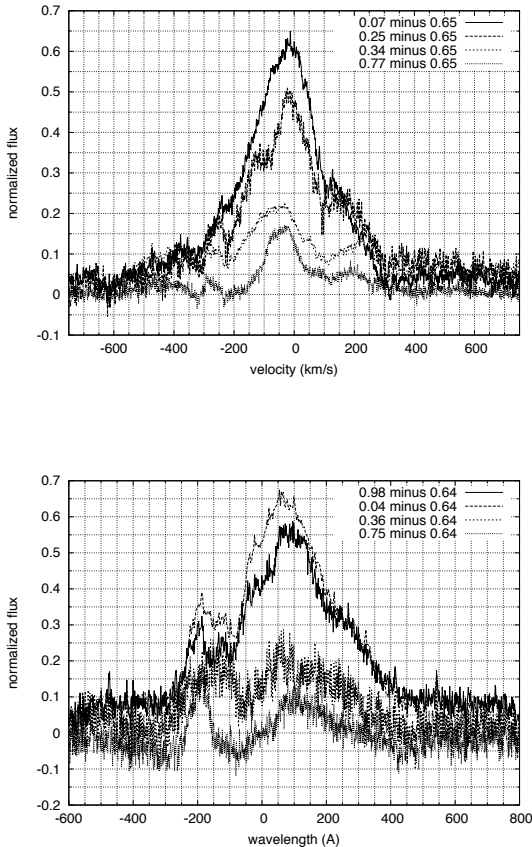


Figure 16. Up: $H\alpha$ difference spectra near $\Phi_o = 0.00$ at selected long cycle phases. Down: $H\alpha$ difference spectra near $\Phi_o = 0.75$ at selected long cycle phases. Velocities are with respect to the system center of mass.

1999) and the comparison of observed and reconstructed line profiles shows the self-consistency of the method.

When interpreting Doppler maps we should keep in mind the difficulty in the representation of optically thick structures and components above or below the orbital plane. This is specially relevant for the Balmer emission lines discussed in this paper. The evidence presented in this section for $H\alpha$ is not conclusive, and the map should be only taken as a particular two-dimensional representation of the three-dimensional mass flows in the binary.

3.9.1 The $H\alpha$ Doppler map

We built the Doppler map for the donor-subtracted $H\alpha$ line with resolution $FWHM = 65 \text{ km s}^{-1}$. Only spectra with $0.8 < \Phi_l < 0.3$ were used, since others showed too weak emission. The map is shown in Fig. 17. The stream path plotted in the map is for a point mass primary. For a $4.4 R_\odot$ primary radius the stream would ultimately collide with the star at tomogram velocities $V_x = -675 \text{ km s}^{-1}$ and $V_y = -310 \text{ km s}^{-1}$ (i.e. in the lower left quadrant) or even sooner with disc or wind.

The $H\alpha$ absorption profile goes below the continuum during some phases. This is inconsistent with an optically thin emission formed in the gas velocity field. Having said that 3 interpretations for the Doppler map remain: (i) the gas is optically thick in the lines, (ii) the photospheric spectrum has a broad absorption component and (iii) a combination of both is present (an optically thick wind and/or disc). The map indicates that the absorption has a $FWZI$ of circa 150 km s^{-1} and has significant radial velocity with phase still consistent with the primary. We computed phased spectrograms and the orbital velocity modulation of the absorption can be confirmed at high state. It is possible to interpret this region as the optically thick circumprimary disc. Additional pieces of information are that the emission almost disappears at L_1 and around $\Phi_o = 0.65$. Finally, emission is detected around the donor, confirming the results inferred from our $H\alpha$ difference spectra. In summary, and taking into account our complementary spectroscopic analysis, the $H\alpha$ Doppler map is consistent (but not conclusive) with an optically thick circumprimary disc plus high-latitude wind and emitting material located around the donor star.

3.9.2 The $Mg \text{ II } 4481$ and $\text{CI } 6588$ Doppler maps

We detected $Mg \text{ II } 4481$ and $\text{CI } 6588$ emissions in the donor subtracted spectra whose velocities indicated an origin around the secondary star. These emission are very variable in intensity and sometimes show double peaks. They are present at high and low state. A renormalization of the continuum was made around these lines and Doppler maps were constructed in the usual way.

The Doppler map for $Mg \text{ II } 4482$ was centered at 4481.2 \AA , it shows that this line is formed in the donor and it is not produced by irradiation of the hemisphere facing the gainer, but probably corresponds to chromospheric activity (Fig. 18). The same result is obtained with the $\text{CI } 6588$ line. The presence of near/underlying absorptions in this line and the data sampling and spectral noise produces strong streaks mimicking emission at L_2 , L_3 and the gas stream region. These are very likely artifacts of the reduction process.

The discovery of chromospheric emissions open the possibility that the donor in $V 393 \text{ Sco}$ possesses a non-neglected magnetic field.

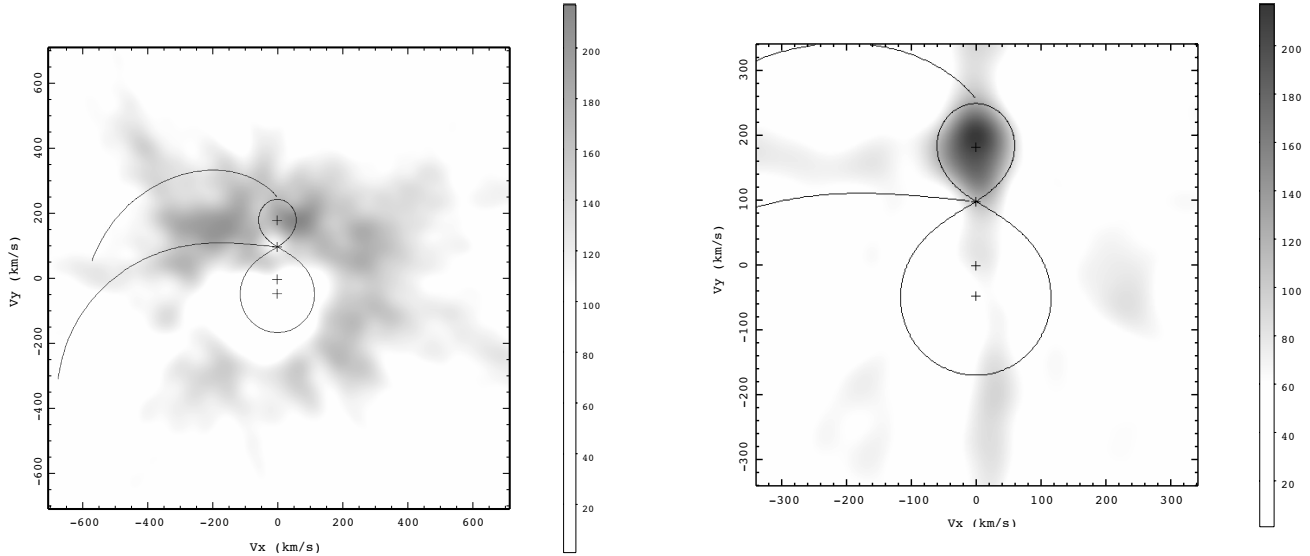


Figure 17. The back-projection Doppler map for the donor-subtracted $H\alpha$ line during high state ($0.8 < \Phi_l < 0.3$). Crosses show, from up to down, donor center of mass, L1 point, system center of mass and gainer center of gravity. Roche lobe surfaces for a point mass gainer are shown along with the gas stream path (lower track). The upper track represents the keplerian velocity of a disc if it would exist along the stream.

3.10 The O I 7773 triplet and the Si II 6347–6371 doublet

The O I 7773 line appears in absorption on low state and almost completely filled by emission on high state. This line is a triplet with the redder component displaced by 67 km s^{-1} and 107 km s^{-1} from the two other components, but in our spectra it appears broadened and the single components are not resolved. The line shows pronounced *blue* absorption wings in the phase range $\Phi_o = 0.55\text{--}0.84$ and enhanced *red* absorption wings during $\Phi_o = 0.20\text{--}0.45$ (Fig. 19). These line depressions are similar to those observed in He I 10830 (M10) and are present even before applying the disentangling process.

We detected Discrete Absorption Components (DACs, of typical depth 3 to 5 % of the continuum intensity) in virtually all O I 7773 spectra with enhanced absorption wings, but in much larger number in the blue wing. DACs are visible even before spectral disentangling and in spectra free of fringes and bad pixel regions. From the above, and from their visibility at specific orbital phases, we argue that DACs are not artifacts of the disentangling process or instrumental setup.

We averaged consecutive spectra taken few minute apart on a same night in order to improve the signal to noise ratio (typically $S/N \approx 120$). Then we measured DAC radial velocities with respect to the reference wavelength $\lambda_0 = 7773.83 \text{ \AA}$. Up to 8 DACs were detected in a single spectrum but more could be present hidden by the waiving continuum. Most DACs are observed with positive velocities during the first half of the orbital cycle but with negative velocities the second half (Fig. 20). We notice that DACs velocities are scattered around the line representing the donor star velocity, and are profusely observed at blue and red wings around $\Phi_o = 0.4$. This is illustrated in the asymmetric distribution observed in DAC radial velocities (Fig. 20). The corresponding distribution of velocities relative to the donor is smooth and relatively symmetric.

Interestingly, we noticed that there is no indication of the

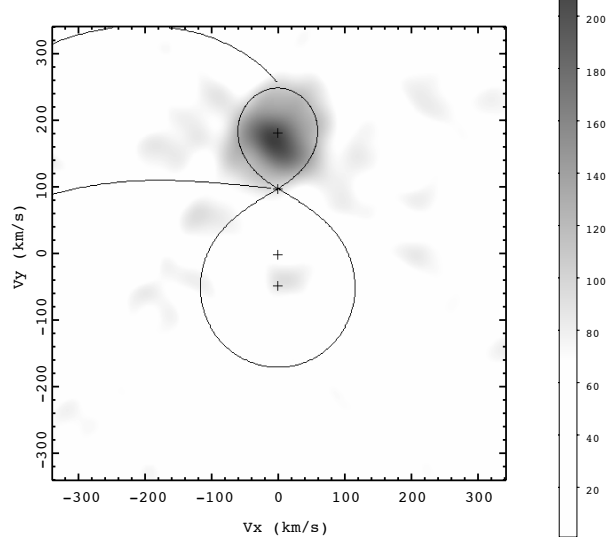


Figure 18. Up: The back-projection Doppler map for the donor-subtracted Mg II 4482 line. Symbols are as in previous figure. The $FWHM$ resolution is 60 km s^{-1} . Down: Same as above but for the C I 6588 line with resolution 40 km s^{-1} .

triplet structure in any of the DACs. In addition, 20% of the DACs are double, with separation between the components of about 45 km s^{-1} . DACs have velocities a few hundreds of km s^{-1} relative to the binary center of mass and are detected at low and high state. It is notable that profiles taken 69 days apart, at $\Phi_o = 0.68$ and $\Phi_l = 0.50$ (HJD 2454672.52566 and 2454703.49230) show roughly the same set of DACs at very similar velocities. At high state discrete emission features appear in the spectra and the identification of DACs is difficult. One is tempted to say that some DACs are replaced by discrete *emission* features at the high state.

Stationary or almost-stationary DACs are observed in the red wing of the line, with velocities 265 and 365 km s^{-1} . These features could correspond to Fe II 7780.4 and Fe II 7783.0 with velocities 12 km s^{-1} relative to the barycenter, but we cannot discard O I “satellite” lines (Fig. 20). Around $\Phi_o = 0.2\text{--}0.3$ the DAC at 365 km s^{-1} (eventually Fe II 7783.0) attains the larger velocity

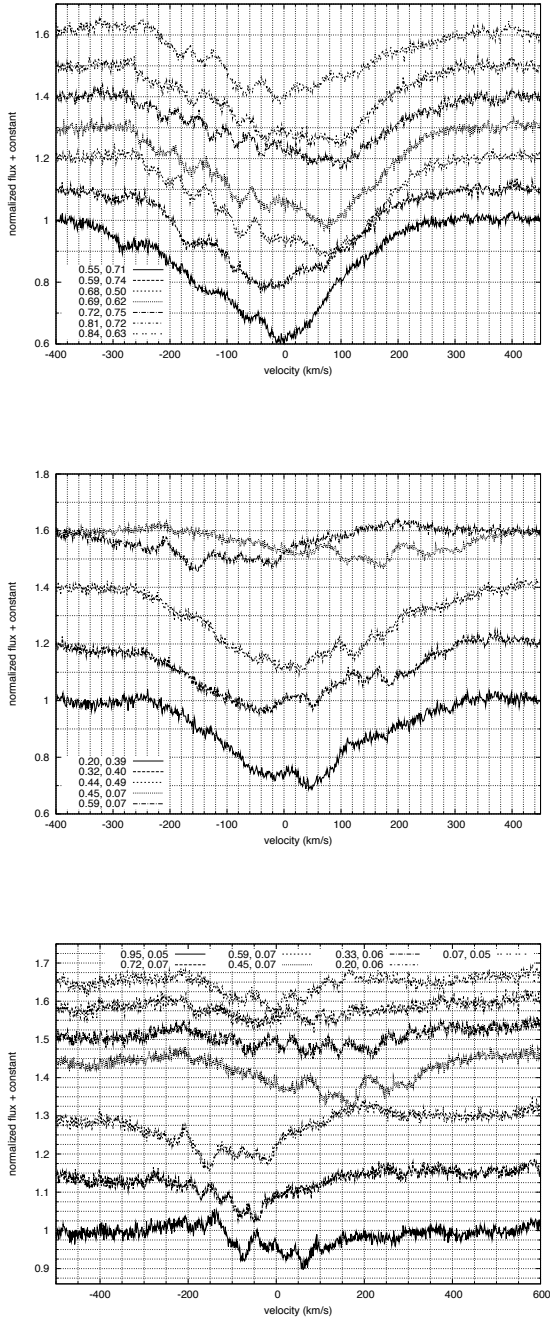


Figure 19. Up: Examples of donor-subtracted OI 7773 lines showing DACs in enhanced blue wing. Middle: Examples of donor-subtracted OI 7773 lines showing DACs in enhanced red wing. Down: Donor-subtracted OI 7773 spectra during the high state. Labels indicate orbital and long-cycle phases.

(470 km s⁻¹ relative to the OI 7773 center) and is wider than in other epochs. In contrast to these almost-stationary features, we notice that some DACs seem to follow, at least at some epochs, quasi-sinusoidal patterns following the donor orbital motion.

The RV of the OI 7773 CA presents a slight orbital oscillation with half-amplitude 32 km s⁻¹ in anti-phase with the donor and center displaced by 5 km s⁻¹ from the systemic velocity. This

behavior changes drastically at long cycle maximum, as seen in Fig. 20, adopting a saw-teeth pattern, with a large velocity (+125 km s⁻¹) prior to $\Phi_o = 0.5$ and a low velocity (-125 km s⁻¹) just after. Difference profiles shown in Fig. 21 indicate that this behavior is the consequence of the disappearance of the red (blue) emission wing during $\Phi_o = 0.45$ (0.59). This phenomenon can be interpreted as the occultation of wind high-velocity regions by the gainer or the disc.

We also find DACs in Si II 6347/6371. The 50% of the DACs detected in Si II 6371 are also detected in Si II 6347. In addition, 44% of the Si II DACs have RV correspondence with those observed concurrently in OI 7773. We find relatively strong stationary lines at 6375.8 Å and 6379.2 Å that we identified with diffuse interstellar bands (Herbig 1975).

Radial velocities of broad donor-subtracted Si II 6347/6371 line profiles present large scatter, but they are roughly in anti-phase with the donor RVs revealing their origin in or around the gainer.

3.11 Enhanced absorption wings

Enhanced absorption wings are observed in several lines, especially OI 7773 (Fig. 19, upper panel) and He I 5875 (not shown). We measured the velocity of the wing edge with respect to the line center resulting in averages of 350 ± 25 (standard deviation) and -350 ± 20 km s⁻¹ for the red and blue wing of OI 7773 and 410 ± 55 and -390 ± 50 km s⁻¹ for the red and blue wing of He I 5875, respectively (Fig. 22). We propose that enhanced absorption wings are caused by photon absorption in the gas stream and circumprimary disc.

Blue depressed wings occur in the range $\Phi_o = 0.5-0.9$, roughly coinciding with the phases when the stream faces the observer, and red enhanced wings in the range $\Phi_o = 0.9-0.45$, just when the observer see the receding stream (the exceptions are the blue wings around $\Phi_o = 0.15$ and the OI red enhanced wings already at $\Phi_o = 0.85$). The blue wing at $\Phi_o = 0.15$ could be explained if part of the stream bounces back after impacting the disc producing blue-shifted additional absorption. This behavior is similar but not strictly the same that the one followed by DACs. In particular, the red enhanced wing appears around $\Phi_o = 0.9$ but at this phase DACs still are present in the blue wing. Another interesting result is the abrupt change between positive and negative velocity, with no smooth transition between them.

4 DISCUSSION

Many of the phenomena described in this paper can be understood in terms of a global mass-loss process involving the transfer of mass between the donor and the gainer. In the following we discuss the spectroscopic variability in terms of possible line forming regions, line forming mechanisms and mass loss/exchange channels. A comprehensive summary of all these issues is given in Table 7.

4.1 The wind revealed in the helium emission

It is unusual to find in a binary star stationary spectral features, since most of the emitting regions should bring the fingerprints of the orbital motion. Therefore the discovery of stationary red emission in He I 6678 is important to constrain the physical scenario. The first thing we notice is that the RV variability of the emission peaks cannot be attributed to the motion of the central absorption feature, as in the case of H α . This feature is in the middle of both

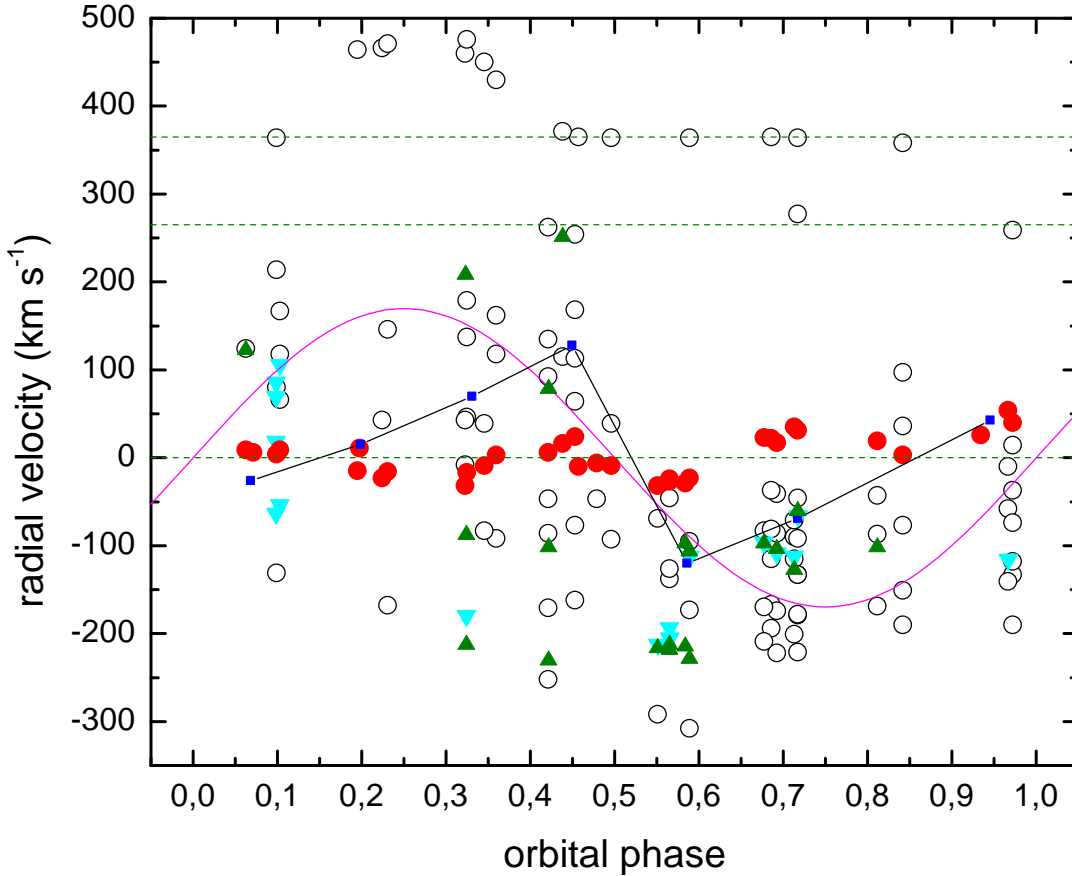


Figure 20. Radial velocities referred to the binary center of mass for DACs (circles) and line center (filled circles for $0.39 < \Phi_l < 0.76$, filled squares for $0.05 < \Phi_l < 0.07$) for the O I 7773 line in UVES spectra. Measurements for Si II 6347 DACs (triangles) and Si II 6371 DACs (inverted triangles) are also shown. The theoretical radial velocity for the donor is shown by a sinusoid and dashed lines of constant velocity 0, 265 and 365 km s^{-1} are also displayed.

Table 7. Summary of spectroscopic variability, possible line forming regions and line formation mechanisms. ABS, CA, EM, RV and SIN stand for absorption, central absorption, emission, radial velocity and sinusoidal, respectively. Bound-bound emission is labeled b-b.

Feature	Variability	Main Region	Mechanism
HI, He I, Si II & O I low velocity EM	Larger at high-state	wind	b-b EM
HI and He I CA depth	Larger at low-state	disc	Self-ABS
HI, He I, Si II & O I CA RV	Quasi-SIN, low amplitude	disc	Self-ABS
Balmer V/R curve	SIN + perturbations on eclipses	wind + disc	Doppler + Eclipses
He I V & R peak RVs	V quasi-SIN, R stationary and shifts at high state	wind	b-b EM
DACs	Mostly in depressed blue wings on 2nd half-cycle	stream?	unknown
Balmer extended EM wings	Red side 1st half-cycle, blue side 2nd half-cycle	wind	photon scattering
Enhanced ABS wings	Complex, mostly blue side 2nd half-cycle	stream + disc	ABS

peaks and seems not influence the RV of the stationary red peak. The more simple explanation for this behavior is assuming an almost stationary broad single emission peak divided by the CA, and that this CA has an important blue wing component perturbing the measurement of the blue emission peak, especially at $\Phi_o = 0.40$, when the perturbation is large. The blue depressed wing could be due to the gas stream facing the observer at this phase and be the

low latitude manifestation of the wind producing the broad helium emission. This wind could be produced by stream deflection at the disc/stream interaction region. Following the same reasoning that for Balmer lines, the helium half-peak separation (up to 450 km s^{-1}) is also consistent with a critically rotating gainer unable to accrete more material.

In principle the helium emission wings could be due to scat-

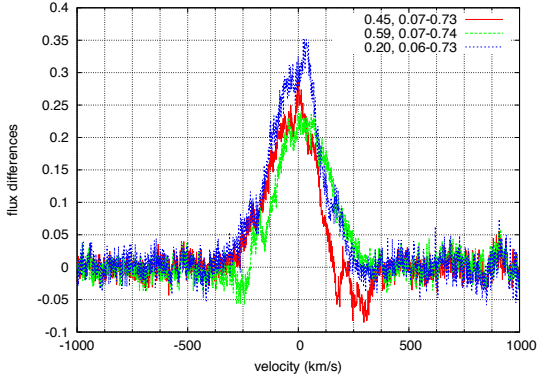


Figure 21. Donor-subtracted OI 7773 difference spectra during epochs of maximum RV shift at long maximum ($\Phi_o = 0.45$ and 0.59) and zero RV shift ($\Phi_o = 0.20$). Labels indicate orbital phase and the difference between the long-cycle phases.

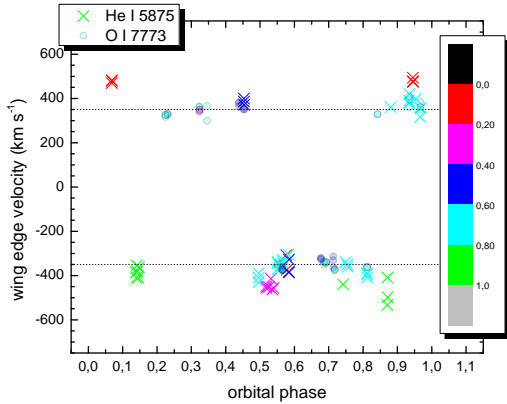


Figure 22. The velocity for the edge of the enhanced wing for OI 7773 and He I 5875 relative to the line center. Averages values for OI 7773 are shown by dotted lines. Color bands indicate Φ_i ranges.

tering and true absorption both in the line and continuum by the Schuster’s mechanism (e.g. Gebbie & Thomas 1968, Israeli & Nikoghossian, 1996). However, it is difficult to explain the asymmetric behavior between blue/red peak under this hypothesis.

The presence of low velocity emission in He I lines confirms our previous view that the wind also emits in helium. As happens for Balmer lines, larger helium emission during the high state implies an increase in wind emissivity during this epoch.

van Rensbergen et al. (2008) claim that gainer’s spin-up and hot spots can drive mass out of a binary. They argue that releasing of accretion energy produces enough energy to sustain a wind from a small stream impact region. Their model gives a physical basis for a mass loss larger than the one driven by winds of isolated single stellar components of V 393 Sco. In addition, the discovery of a chromospherically active donor suggests that magnetism could play a role as a wind driver mechanism. The symmetry of the binary configuration regarding the orbital plane indicates that this wind should be bipolar.

4.2 Balmer extended emission wings and the stream/disc interaction

The presence of extended emission wings (EEWs) in some Balmer lines beyond $\pm 2000 \text{ km s}^{-1}$ cannot be attributable to emission from a Keplerian disc. We notice that the wind projected velocities (hundreds of km s^{-1}) are too low to explain EEWs by electronic recombination, and that the mechanism of Thompson scattering could produce extended emission wings as occurs in Be stars (Poeckert & Marlborough 1979) and the luminous blue variable AG Car (Schulte-Ladbeck et al. 1994). EEWs appear in the red wing on the 1st half-cycle and in the blue wing on the 2nd half-cycle so the forming medium shares the same orbital variability that the medium responsible for DACs and enhanced absorption wings. However, we notice that the emission features require a medium at latitudes higher than absorbing material. This suggests that part of the stream is deflected by the disc towards high latitudes producing high density regions responsible for the Thompson scattering and EEWs. All of this activity occurs principally at the 1st and 2nd binary quadrant.

4.3 Optically thick disc, hot spot and gas stream

The central absorption cores of the lines studied in this paper are probably produced in the gainer pseudo-photosphere, modeled by M12 as an optically-thick disc. The temperature inferred for the disc from spectroscopic line ratios $T_{hot} = 16.000 \text{ K}$ coincides with those inferred from the light curve analysis. The orbital behavior of line cores is consistent with light-centers placed somewhere along the line joining the stellar centers near the gainer. Variations in the depth of the CAs are explained by changing amounts of filling emission as the wind increases its strength at high state.

The gas stream is revealed at $\Phi_o = 0.9$ in the He I *FWHM* maximum and in the asymmetries observed in OI and He I lines (Section 3.11). The hot spot, on the other hand, shows up in the “z-wave” of the $H\alpha$ *V/R* variability.

4.4 Line emission: the optically thin high latitude wind and donor activity

The increase of line emissivity during eclipses and the sustained emission increase at low velocities during high state strongly suggest that most of the low velocity Balmer emission comes from electronic recombination at the high latitude wind. The same occurs for the emission seen in OI 7773 and the Si II doublet. As discussed in Section 3.7.2 part of the $H\alpha$ emission also comes from the disc outer edge and a region around the donor. It is remarkable that when the system approaches the high state the line emission increases in the wind (the low velocity region) and around the donor (Fig. 16). This finding suggests a connection between the wind strength and the activity responsible for the line emission around the donor. This possible connection will be explored in a forthcoming paper dedicated to the study of weak emission features detected in the residual spectra. So far, Doppler maps show that the Mg II 4481 and CI 6588 residual emissions are formed in a chromospherically active star. This finding arises the possibility of a magnetically active secondary in V 393 Sco.

4.5 The DAC/stream connection

We find that DACs follow the pattern of the enhanced absorption wings, so a connection between DACs and the gas stream is possi-

ble (see Sects. 3.10 and 3.11). The narrowness of DACs ($FWHM$ a few tens of km s^{-1}) indicates that they are formed in a different medium than the main OI7773 line. Here we propose, tentatively, that DACs can be identified with tracers of donor mass loss. Traditionally, a continuum mass stream is considered the output of Roche-lobe overflow. However, the presence of DACs could reveal a stream composite of discrete and relatively narrow mass flows following magnetic field lines connecting the donor with the disc. In this view, DACs could be due to Zeeman splitting of absorption lines produced in streams projected against a bright continuum. The presence of discrete emissions on high state could indicate a re-ordering of the streams, carrying material by high latitudes producing emission rather than absorption lines. The orbital distribution of DAC RVs could be result of the complex structure of the magnetic field.

In order to support the above interpretation we notice that: (i) Zeeman splitting has been reported in the Si II doublet of the related interacting binary β Lyrae (Skulskij & Plachinda 1993), (ii) the transient radio nature of V 393 Scorpii has been interpreted in terms of a stellar coronal magnetic field $B \approx 10^2$ G (Stewart et al. 1989), (iii) our discovery of a chromospherically active donor suggests a magnetic donor star and (iv) the discovery of a large and *stable* coronal loop observed in Algol and RY Vul (Peterson et al. 2010, Richards et al. 2010) indicates that evidence for magnetically channeled streams has been found in DPV-related interacting binaries. From the theoretical point of view, the physical basis for the donor magnetism might be its rapid synchronous rotation, that might generate a dynamo-powered magnetic field. This idea has been explored and vindicated for Algols with late-type components (e.g. Sarna et al. 1998, Moss & Tuominen 1997) and for rapidly rotating A-type stars (Featherstone et al. 2009).

At present the nature of DACs is obscure, but our findings provide strong observational constraints for any competent model, and suggest that spectropolarimetry could be a successful technique in the diagnostic of the feature's splitting.

4.6 New insights on the long photometric cycle

In the past sections we have presented evidence for the existence of several circumstellar regions in V 393 Sco; an optically thick disc-like pseudo-photosphere, a gas stream, a hot spot, a chromospherically active secondary star and a high-latitude wind revealed in almost stationary Balmer and He I emission. We propose that all these regions and their associated phenomena indicate the presence of a mass-loss phenomenon in V 393 Sco that is cyclically modulated with the long period. In this section we explore possible causes for this variability.

4.6.1 On the possibility of a dynamically perturbed disc

Considering that dynamically perturbed discs are found in other close binary systems, we have analyzed the possibility that the long cycle is produced by a tilted circumprimary disc whose normal axis precesses around the rotational axis of the gainer. In this case we should observe deeper CA when the disc edge hides the gainer, and shallower CA when a larger projected disc area is observed. However, a tilted disc hypothesis presents severe problems: (i) it should produce large orbital changes in the equivalent width of the emission lines proportional to the projected area and also large changes in the peak separation at high state, which are not observed, (ii) it is difficult to imagine how the optically thick disc might emit at

Balmer lines and (iii) the hypothesis is not consistent with the stability of the orbital LC solution (M12). In addition, the constancy of the V/R light curve at high and low state strongly argues against large scale dynamical perturbations including disc precession or disc wrapping. Beside the previous evidence, the conclusion that the light source of the long-cycle is not eclipsed (M12) is not compatible with the perturbed disc hypothesis.

4.6.2 The cyclic wind and the long cycle

We have found evidence that the long cycle in V 393 Scorpii is produced by a wind injecting larger amounts of mass into the circumbinary medium at high state. This conclusion is in agreement with the suggestion given by M12 that circumbinary material is responsible for the extra light during the high state. These authors give $9 \times 10^{-9} M_{\odot}/\text{yr}$ for the mass transfer rate which means that $6.2 \times 10^{-9} M_{\odot}$ are injected into the interstellar medium every long cycle in steady state regime. This extra mass produces additional line emission in low projected velocities and also additional continuum light by free-free emission. In this view it is the changing wind that produces the long photometric cycle. The simultaneous increase in $H\alpha$ line emissivity near the donor and the gainer suggests a connection between the wind and the chromospherically active donor star. The wind could be caused by stream deflection at the disc hotspot. The possibility of magnetic fields connecting the donor and the disc and eventually powering the wind deserves to be studied, especially knowing that the binary is a transient radio source (Stewart et al. 1989).

It is possible that the final cause for the long cycle is self-modulation of the mass transfer rate. As the gainer is rotating at critical rotation it cannot accumulate the extra mass received from the donor and this mass is finally expelled by the wind. Spectroscopy shows that the high and low states in V 393 Sco correspond to changes in line and continuum emissivity, and probably density, of the wind, which could reflect changes in the mass transfer rate. Let's assume that the mass transfer rate is modulated by the photon flux arriving from the gainer. This flux is attenuated by intervening material when the wind is stronger, producing less irradiation flux and lower \dot{M}_2 . This produces a decrease in wind strength and subsequently larger irradiation flux, bigger \dot{M}_2 and so on. This valve mechanisms could explain the long cycle, but theoretical work is needed to demonstrate that it is a valid mechanism and stable on the long term, beside of taking into account the observational evidence indicating a chromospherically active rather than an irradiated donor.

The wind discovered in V 393 Sco might be driven by the same (still unknown) physical mechanism that the wind found in β Lyrae (Harmanec et al. 1996), but there are differences between β Lyrae and V 393 Sco that have been pointed out by M12. These authors propose that β Lyrae is in an earlier evolution stage than V 393 Sco, and characterized by a larger mass transfer rate.

4.6.3 On equatorial and polar outflows

Our earlier claim for equatorial mass flows in V 393 Sco (M10) can now be tested with our new optical spectroscopic dataset. Our data suggest that line asymmetries, especially those seen around $\Phi_o = 0.5$ and previously interpreted as equatorial mass flows through the L3 point, are part of a more complex orbital pattern. Although in this paper we have studied the asymmetries of the OI7773 and He I5875 lines and M10 those of the He I1083

nm line, it is reasonable to assume that all these lines behave similarly during the orbital cycle. The new datasets show that the blue depressed wing remains during large part of the 2nd half cycle and cannot be interpreted in terms of an L3 outflow only (Fig. 22). The new pattern is best explained in terms of an anisotropic wind, emerging near the system barycenter in direction of the binary motion. On the other hand, the interpretation of the red depressed wing near $\Phi_o = 0.9$ and 0.1 in terms of gas stream infall remains solid in this study, but the new observation of blue depressed wings around $\Phi_o = 0.15$ is puzzling. A possible explanation for this feature is detection of material bouncing back from the stream/disc impact region.

M10 favored equatorial mass flows as the cause for the long cycle in part due to the absence of long cycle variability in UV superionized lines. The resonance lines of Si IV, C IV and N V do not seem to be associated to the long-cycle phenomenon. It is then possible that these lines are formed in the stellar wind emerging from polar regions of the B-type gainer (as revealed by line asymmetries discussed by M10), but probably this *polar-wind* is not related to the *disc-wind* discussed in this paper, that is clearly involved in the long-cycle variability. The IUE observations are limited to only a few spectra, this unfortunate constraint impedes to have a clear picture of superheated regions during the long-cycle.

5 CONCLUSIONS

In this paper we have analyzed high resolution optical spectroscopy of V 393 Sco with time resolution suitable for studying independently the orbital and long cycle variability. In general, the spectroscopic variability can be explained in terms of several circumstellar zones including a circumprimary disc, a gas stream, a hot spot and a modulated high latitude wind. We have shown that the long cycle is the manifestation of this variable wind, probably produced by the interaction of the gas stream and the optically thick disc surrounding the critically rotating B-type primary. Our main conclusions are:

- We detected the donor in our spectra; its effective temperature was determined from a comparison with theoretical synthetic spectra, obtaining $T_2 = 7900$ K. The donor RV was measured and the orbital elements determined; they are given in Table 5. We find a significant small orbital eccentricity for the system, but its meaning is not clear in an interacting binary with mass flows.
- From the strength of diffuse interstellar bands we estimate $E(B - V) = 0.15 \pm 0.05$, consistent with the M10 result.
- We developed a method of spectral disentangling subtracting from every spectrum at every observing epoch the donor synthetic spectrum weighted by its fractional contribution given by our light curve model. This method turned to be adequate to remove the main spectral features of the donor and for studying the remaining components of the system.
- At low stage the He 4471 and Mg 4481 equivalent widths are consistent with line formation in an optically thick region with temperature 16.000 K. We argue that at low state these lines are less contaminated by emission and probe the pseudo-photosphere of the B-type gainer.
- Residual spectra reveal several metallic emission lines from the donor, like Mg II 4481 and C I 6588. Doppler maps of these lines reveal a homogeneously-distributed emissivity around the secondary, not compatible with irradiation-induced emission but with a chromospherically active star. The highly variable nature

of this emission along with the reported radio-transient nature of the binary rise the question on the probable magnetic nature of the donor.

- Novel spectral features were detected: discrete absorption components (DACs), especially visible at blue-depressed O I 7773 absorption wings during the second half-cycle, Balmer double emission with V/R curves showing “z-type“ and “s-type“ excursions around secondary and main eclipse, respectively, and H β emission wings extending up to ± 2000 km s $^{-1}$.

- DACs are a new and still enigmatic phenomenon; deeper studies are needed to enlightening the nature of these features. We suggest that DACs could be Zeeman separated absorption lines formed in magnetized gas streams. This conjecture can be tested with spectropolarimetry.

- Line asymmetries can be interpreted in terms of photon absorption in the canonical gas stream, a large-scale wind and material bouncing back from the stream/disc impact region.

- We notice that the relatively large widths of the Balmer and helium absorption cores are consistent with rotational broadening in absorbing material around a critically rotating gainer.

- Balmer and He I emission are not eclipsed and in average the H α violet peak is larger than the red one. At phases of maximum disc visibility and on high state the emission profiles are single-peaked. These findings suggest that Balmer and He I emission are produced in a high-latitude bipolar wind.

- The extended Balmer emission wings can be the result of Thompson scattering in dense regions of this wind. These regions are in the binary hemisphere containing the stream-disc interaction region and could be formed by stream deflection at the hot spot.

- As cause for the long cycle we exclude a dynamical instability like disc precession or disc wrapping. This conclusion is based on the stability of the V/R curve, the stability of the photometric orbital light curve, the variability of spectral features like peak separation and most importantly the fact that the long cycle is produced by a non-eclipsed source.

- We interpret the long-cycle in terms of a bipolar wind whose emissivity is modulated with the long period. This wind produces rather stationary Balmer, O I, Si II and He I broad emissions. On high state the wind strength is larger than on low state. We argue that an increase in wind strength is the cause for the larger line emission and brighter and redder continuum on the high state.

- It is very likely that the wind is the result of the interaction between the gas stream and the optically thick and massive circumprimary disc. A donor magnetic field could play an important role in the energetic of the phenomenon and acting as a driving mechanism for the wind.

6 ACKNOWLEDGMENTS

We acknowledge an anonymous referee for valuable comments that helped to improve the first version of this manuscript. REM acknowledges support by Fondecyt grant 1070705, 1110347, the Chilean Center for Astrophysics FONDAF 15010003 and from the BASAL Centro de Astrofísica y Tecnologías Afines (CATA) PFB-06/2007. G. D. gratefully acknowledge the financial support of the Ministry of Education and Science of the Republic of Serbia through the project 176004, Stellar physics.

REFERENCES

- Bevington P. R., Robinson D.K., 1992, in *Data Reduction and Error Analysis for the physical Sciences*, second ed., New York: McGraw-Hill
- Castelli, F. & Hubrig, S., 2004, *A&A*, 425, 263
- Charbonneau P., 1995, *ApJS*, 101, 309
- Eggleton P., 2006, *Evolutionary Processes in Binary and Multiple Stars*, edited by Peter Eggleton, Cambridge, UK, Cambridge University Press.
- Featherstone N. A., Browning M. K., Brun A. S., Toomre J., 2009, *ApJ*, 705, 1000
- Gebbie K. B., Thomas R. N., 1968, *ApJ*, 154, 285
- Harmanec P., et al., 1996, *A&A*, 312, 879
- Herbig G. H., 1975, *ApJ*, 196, 129
- Israelian G., Nikoghossian A., 1996, *QJST*, 56, 509
- Kreiner J. M., 2004, *AcA*, 54, 207
- Kurucz, R., 1993, CD-ROM 18
- Lucy L. B., 2005, *A&A*, 439, 663
- Marsh T. R., Horne K., 1988, *MNRAS*, 235, 269
- Mennickent R. E., Djurasevic G., Kolaczowski Z., Michalska G., 2012, *MNRAS* in press.
- Mennickent R. E., Kolaczowski Z., Graczyk D., Ojeda J., 2010a, *MNRAS*, 405, 1947
- Mennickent R., Kolaczowski Z., Djurasevic G., Michalska G., Barría D., 2010b, *Stellar Populations Planning for the Next Decade, Proceedings of the International Astronomical Union, IAU Symposium, Volume 262*, 392
- Mennickent R., Kolaczowski Z., 2010, *Binaries - Key to Comprehension of the Universe. Proceedings of a conference held June 8-12, 2009 in Brno, Czech Republic. Edited by Andrej Prša and Miloslav Zejda. ASPC*, 435, 283
- Mennickent R. E., Kolaczowski Z., Michalska G., Pietrzyński G., Gallardo R., Cidale L., Granada A., Gieren W., 2008, *MNRAS*, 389, 1605
- Mennickent R. E., Cidale L., Díaz M., Pietrzyński G., Gieren W., Sabogal B., 2005, *MNRAS*, 357, 1219
- Mennickent R. E., Pietrzyński G., Diaz M., Gieren W., 2003, *A&A*, 399, L47
- Mennickent R. E., Diaz M. P., Arenas J., 1999, *A&A*, 352, 167
- Moss D., Tuominen I., 1997, *A&A*, 321, 151
- Munari U., 2000, *Molecules in Space and in the Laboratory, Proceedings of a workshop held 2-5 June 1999 in Carloforte, Cagliari. Edited by I. Porceddu, and S. Aiello. Bologna, Italy: Italian Physical Society, Conference Proceedings*, v. 67, 179
- Peters G. J., 2001, *proceedings of "The Influence of Binaries on Stellar Population Studies"* ed. D. Vanbeveren (Kluwer), *Astrophysics and space science library (ASSL)*, Vol. 264, 79
- Peters G. J., Polidan R. S., 1984, *ApJ*, 283, 745
- Peterson W. M., Mutel R. L., Güdel M., Goss W. M., 2010, *Nature*, 463, 207
- Pilecki B., Szczygiel D. M., 2007, *IBVS*, 5768, 1
- Poleski R., Soszyński I., Udalski A., Szymański M. K., Kubiak M., Pietrzyński G., Wyrzykowski Ł., Ulaczyk K., 2010, *AcA*, 60, 179
- Poekert R., Marlborough J. M., 1979, *ApJ*, 233, 259
- Richards M. T., 2004, *AN*, 325, 229
- Richards M. T., Sharova O. I., Agafonov M. I., 2010, *ApJ*, 720, 996
- Rosenfeld A., Kak A. C., 1982, *Digital picture processing*, AP
- Sbordone, L., 2005, *MSAIS*, 8, 61
- Sarna M. J., Yerli S. K., Muslimov A. G., 1998, *MNRAS*, 297, 760
- Schulte-Ladbeck R. E., Clayton G. C., Hillier D. J., Harries T. J., Howarth I. D., 1994, *ApJ*, 429, 846
- Skul'Skij M. Y., Plachinda S. I., 1993, *AstL*, 19, 203
- Stewart R. T., Slee O. B., White G. L., Budding E., Coates D. W., Thompson K., Bunton J. D., 1989, *ApJ*, 342, 463
- van Rensbergen W., De Greve J. P., De Loore C., Mennekens N., 2008, *yCat*, 348, 71129
- Weselak T., Galazutdinov G. A., Musaev F. A., Kretowski J., 2008, *A&A*, 484, 381
- Zahn J.-P., 1977, *A&A*, 57, 383
- Zahn J.-P., 1975, *A&A*, 41, 329

This paper has been typeset from a \TeX / \LaTeX file prepared by the author.